Quantifying transient binding of ISWI chromatin remodelers in living cells by pixel-wise photobleaching profile evolution analysis

Fabian Erdel[1] and Karsten Rippe[1]

Research Group Genome Organization and Function, Deutsches Krebsforschungszentrum (DKFZ) and BioQuant, 69120 Heidelberg, Germany

AUTHOR SUMMARY

Our understanding of the dynamic properties of cells is skewed, because measurements in living cells conducted by imaging-based techniques typically have a time resolution of seconds or more. However, many processes in cells, and particularly interactions of proteins with the genome, occur in time frames of less than a second (1). To study fast and slow processes simultaneously from milliseconds to minutes in living cells, we introduce here a fluorescence microscopy-based method termed pixel-wise photobleaching profile evolution analysis (3PEA). It increases the time resolution of approaches that rely on bleaching of fluorescently tagged proteins to evaluate their intracellular mobility. This is achieved by explicitly accounting for the raster scan process inherent to confocal laser scanning microscopy (CLSM). The 3PEA method yields information about processes that occur within milliseconds by measuring a cell for less than 1 s, making it suitable for microscopy-based high-content screening of molecular mobility. The 3PEA approach is generally applicable to studies of protein mobility and interactions in living cells but was developed for dissecting the interactions of a specific class of proteins in the cell nucleus, namely, the chromatin remodelers Snf2H and Snf2L from the imitation switch (ISWI) protein family. These ATP-driven molecular motors rearrange chromatin, the complex of genomic DNA with the associated histone proteins, to regulate DNA compaction and accessibility. Snf2H and Snf2L can change the chromatin conformation in vitro within several seconds (2). In the nucleus, they bind transiently to chromatin, which is important for fast identification of target sites that require their activity (3). To understand how they remodel chromatin in living cells, it is essential to determine their chromatin interaction times in different states. This information can be obtained by measuring the reduction of the protein's free mobility due to binding to the mostly immobile chromatin scaffold using various approaches, such as fluorescence recovery after photobleaching or fluorescence correlation spectroscopy, that provide complementary information (4). These currently used techniques are extended by 3PEA, which is particularly suited to dissect protein–chromatin interactions on time scales between 1 ms and 1 s with a standard CLSM setup.
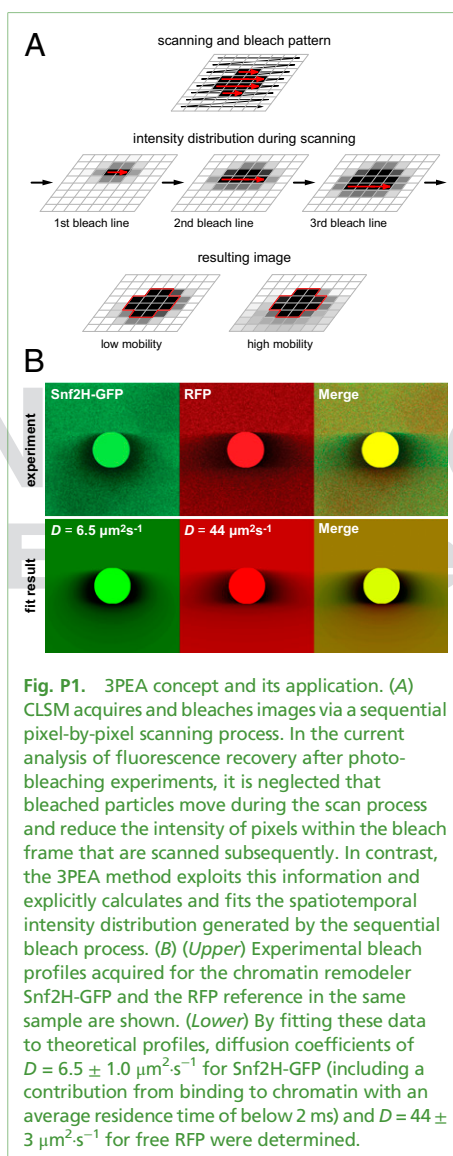
Fig. P1. 3PEA concept and its application. (*A*) CLSM acquires and bleaches images via a sequential pixel-by-pixel scanning process. In the current analysis of fluorescence recovery after photobleaching experiments, it is neglected that bleached particles move during the scan process and reduce the intensity of pixels within the bleach frame that are scanned subsequently. In contrast, the 3PEA method exploits this information and explicitly calculates and fits the spatiotemporal intensity distribution generated by the sequential bleach process. (*B*) (*Upper*) Experimental bleach profiles acquired for the chromatin remodeler Snf2H-GFP and the RFP reference in the same sample are shown. (*Lower*) By fitting these data to theoretical profiles, diffusion coefficients of $D = 6.5 \pm 1.0 \ \mu m^2 \cdot s^{-1}$ for Snf2H-GFP (including a contribution from binding to chromatin with an average residence time of below 2 ms) and $D = 44 \pm 3 \ \mu m^2 \cdot s^{-1}$ for free RFP were determined.

The method is based on the comprehensive evaluation of the time structure of confocal images that are acquired pixel by pixel (Fig. P1). Individual pixels are sequentially illuminated and interrogated in a raster scan process. Thus, every pixel is acquired at a unique time point, which has been exploited previously by correlating intensity fluctuations in different pixels that arise due to particle translocations during imaging (5). A conceptually similar approach can be applied to the process of locally bleaching a region of the image, which occurs in the same pixel-by-pixel manner as the subsequent image acquisition process. The only difference is that the excitation laser intensity is largely increased within the bleach region (Fig. P1*A*, red arrows). The information about translocations that occur within milliseconds is present in the pixel intensity profile of the bleach frame and originates from bleached particles that, during scanning, translocate into regions where they subsequently attenuate the fluorescence signal. This is depicted for particles with high or low mobility in Fig. P1*A*.

The 3PEA approach introduced here explicitly calculates and fits the spatiotemporal intensity distribution generated by the sequential bleach process. It can analyze the bleach image and subsequently acquired postbleach images in the same manner, yielding information on different time scales. We were able to quantitate the transient chromatin interactions of the ISWI-type chromatin remodelers analyzing exclusively the bleach frame. As a reference for proteins that do not interact with chromatin, the isolated green (GFP) and red (RFP) autofluorescent protein domains and

a GFP pentamer were used. An exemplary comparison of experimental and calculated bleach images for Snf2H-GFP and free RFP is shown in Fig. P1*B*. Our 3PEA analysis of Snf2H, Snf2L, and the inactive splice variant Snf2L+13 revealed that these proteins move with effective diffusion coefficients of 5.5–6.5 $\mu m^2 \cdot s^{-1}$ and, on average, bind to chromatin for less than 2 ms. Thus, within 1 s, an ISWI remodeler translocates through almost the whole cell nucleus in a random walk and transiently binds to more than 300 nucleosomes, the complexes of histone proteins, and DNA. This type of nonproductive chromatin sampling during the target search process is well separated from the rare long-lived interactions that involve conformational changes, ATP hydrolysis, or both. These findings support the conclusion that Snf2H and Snf2L do not translocate nucleosomes during most of their chromatin interaction events in the G1 phase of the cell cycle.

The 3PEA method can determine mobility and interaction parameters at high temporal resolution within measurement times of about 1 s with a commercial CLSM setup. This is at least an order of magnitude faster than current methods for mobility measurements, and comparable to the time required for standard imaging. Thus, 3PEA provides a number of unique possibilities for the analysis of protein mobilities during highly dynamic cellular processes as well as the acquisition of protein mobility maps within a single cell, and could be implemented in an automated high-throughput setup. The use of reversible photoswitching instead of bleaching would give the opportunity to perform multiple 3PEA cycles in a single cell to record spatially resolved mobility data in real time. This is particularly relevant for the analysis of fast cellular responses to perturbations like drug treatment or viral infection, and opens up the opportunity to use molecular mobility as an additional readout in various microscopy-based assays.

1. Hager GL, McNally JG, Misteli T (2009) Transcription dynamics. *Mol Cell* 35(6):741–753.
2. Blosser TR, Yang JG, Stone MD, Narlikar GJ, Zhuang X (2009) Dynamics of nucleosome remodelling by individual ACF complexes. *Nature* 462(7276):1022–1027.
3. Erdel F, Schubert T, Marth C, Längst G, Rippe K (2010) Human ISWI chromatin-remodeling complexes sample nucleosomes via transient binding reactions and become immobilized at active sites. *Proc Natl Acad Sci USA* 107(46):19873–19878.
4. Mazza D, Abernathy A, Golob N, Morisaki T, McNally JG (2012) A benchmark for chromatin binding measurements in live cells. *Nucleic Acids Res* 40(15):e119.
5. Digman MA, et al. (2005) Measuring fast dynamics in solutions and cells with a laser scanning microscope. *Biophys J* 89(2):1317–1327.

Erdel and Rippe

Quantifying transient binding of ISWI chromatin remodelers in living cells by pixel-wise photobleaching profile evolution analysis

Fabian Erdel[1] and Karsten Rippe[1]

Research Group Genome Organization and Function, Deutsches Krebsforschungszentrum (DKFZ) and BioQuant, 69120 Heidelberg, Germany

Interactions between nuclear proteins and chromatin frequently occur on the time scale of seconds and below. These transient binding events are important for the fast identification of target sites as concluded from our previous analysis of the human chromatin remodelers Snf2H and Snf2L from the imitation switch (ISWI) family. Both ATP-driven molecular motor proteins are able to translocate nucleosomes along the DNA and appear to exert this activity only on a small number of nucleosomes to which they bind more tightly. For mechanistic studies, one needs to distinguish such translocation reactions or other long-lived interactions associated with conformational changes and/or ATP hydrolysis from nonproductive chromatin sampling during target search. These processes can be separated by measuring the duration of nucleosome binding with subsecond time resolution. To reach this goal, we have developed a fluorescence bleaching technique termed pixel-wise photobleaching profile evolution analysis (3PEA). It exploits the inherent time structure of confocal microscopy images and yields millisecond resolution. 3PEA represents a generally applicable approach to quantitate transient chromatin interactions in the 2- to 500-ms time regime within only ~1 s needed for a measurement. The green autofluorescent protein (GFP)-tagged Snf2H and Snf2L and the inactive Snf2L+13 splice variant were studied by 3PEA in comparison to the isolated GFP or red autofluorescent protein and a GFP pentamer. Our results reveal that the residence time for transient chromatin binding of Snf2H and Snf2L is <2 ms, and strongly support the view that ISWI-type remodelers are only rarely active in unperturbed cells during G1 phase.

fluorescence recovery after photobleaching (FRAP) | nucleosome translocation | protein–chromatin interactions | mobility imaging

Many nuclear proteins bind chromatin with surprisingly short residence times on the time scale of seconds and below. This appears to be a general feature required for an efficient search process of factors that need to find specific sites on chromatin as discussed in a number of reviews (1–3). Such a "continuous sampling" type of target location mechanism is characteristic for imitation switch (ISWI) chromatin remodelers as concluded from our previous analysis (3–5). The ISWI family consists of two ATPases, Snf2H and Snf2L, in humans, which assemble into different complexes via association with additional subunits (6, 7). Their ATP-coupled activity repositions nucleosomes on the DNA, which represents an important activity during DNA replication, repair, and transcriptional regulation. Because only a few percent of Snf2H and Snf2L proteins interact with chromatin for more than 500 ms, it appears that in the cell, they translocate only a small subset of nucleosomes to which they bind tightly (4).

As reviewed previously (8), the available repertoire of methods for measuring chromatin interactions either evaluates the redistribution of bleached particles as in fluorescence recovery after photobleaching (FRAP) (9, 10), or uses the correlation between intensity fluctuations. The latter is referred to as fluorescence correlation spectroscopy (FCS) and measures the mobility from fluorescence intensity fluctuations generated by molecules moving in and out of the observation volume (11). Alternatively,

in spatiotemporal image correlation spectroscopy (STICS), raster image correlation spectroscopy (RICS), or the pair correlation approach (12–14) intensity fluctuations in different pixels of the fluorescence microscopy image are analyzed. Bleaching and correlation methods provide complementary information on protein mobility and interactions (8).

The current implementation of FRAP analyzes the fluorescence recovery within the postbleach image series to obtain particle mobility. It is well suited to study proteins that have a relatively low mobility or are even immobilized during the time of the measurement. The temporal resolution of FRAP is limited by the acquisition speed of the microscope and the time required for efficient bleaching, which is on the 100-ms time scale for most commercial confocal laser scanning microscopes (CLSMs) like the one used in the present study. In contrast, FCS, STICS, and RICS have better time resolution down to microseconds but can only measure proteins with a relatively high mobility because they are based on evaluating intensity fluctuations that arise from the movement of fluorescent molecules in and out of the observation volume. The application of FCS to quantitate protein binding to chromatin is limited for two reasons. First, in all instances we have studied, chromatin dynamics (and possibly other events that lead to the translocation of nuclear subcompartments) detected via bound fluorescent proteins manifest themselves as additional fluctuations of fluorescence intensity with apparent diffusion times in the range of 10–500 ms (4, 15). This contribution needs to be accounted for in the data analysis and can obscure binding events on the same time scale. Second, FCS cannot be applied when proteins are immobilized for several 100 ms because photobleaching becomes significant. However, nuclear proteins display heterogeneous interactions with chromatin, e.g., both subsecond transient binding and high-affinity interactions during which the protein is typically bound in the range of several 100 ms up to minutes (16). Because the latter type of interaction is frequently considered to reflect a biologically important state, and due to the relatively simple experimental setup, most of the recent studies of nuclear dynamics have relied on FRAP. However, the associated kinetic analysis of transient interactions by FRAP is fraught with difficulties due to comparably low temporal resolution (corresponding to the frame time of the microscope) and noninstantaneous bleaching, as well as uncertainties with respect to the effective bleach spot size and shape (17, 18). Even the intracellular diffusion coefficient of an

---

inert protein, such as red autofluorescent protein (RFP) or green autofluorescent protein (GFP), commonly used as a reference cannot easily be determined in a spatially resolved manner by regular FRAP with many commercial systems. The reason for this is the relatively high mobility of these autofluorescent protein domains with diffusion coefficients above 20 μm²·s⁻¹ as derived from FCS measurements in the cytoplasm and the nucleus (19).

Because FRAP and FCS experiments are carried out on different length scales (FCS: ~0.3 μm, FRAP: >1 μm), scale-dependent phenomena, such as anomalous diffusion or caging effects of the nuclear environment, will affect FRAP and FCS experiments differently. Moreover, reaction-diffusion processes exhibit different properties depending on which time scale is used to study them. This makes the integration of data from the two methods difficult, and the cross-validation of FRAP and FCS experiments is limited to the time regime that is accessible to both techniques (8, 15, 20). Our previous combination of FRAP and FCS measurements of ISWI chromatin remodelers delineated chromatin residence times for transient binding to a relatively large time interval from 1 to 500 ms (4), but no single method was found to be suited to measure both fast and slow processes robustly in the same experiment. Furthermore, the regime between the maximum residence time of 500 ms determined by FRAP and the dwell time of 1–2 ms determined by FCS is hardly accessible by both methods. Nevertheless, the accurate determination of transient binding times is crucial to separate chromatin sampling interactions from productive slower binding events that involve conformational changes of the nucleosome or the remodeler as well as ATP hydrolysis. In in vitro experiments, reaction rates of 0.2–0.5 s⁻¹ for ATP hydrolysis and 0.2–13 bp·s⁻¹ for nucleosome translocation were determined for Snf2H and other chromatin remodelers (21–24). Although the upper limit of 500 ms reaction time in living cells could still be compatible with ATP hydrolysis, and possibly also with a translocation step, the dwell time of 1–2 ms measured by FCS can be associated with unproductive binding reactions. Thus, analyzing the 1- to 500-ms regime in a single measurement at high spatial resolution would provide valuable mechanistic information on the mode of interaction between ISWI remodelers and their chromatin substrate.

Here, we address this issue by introducing a fluorescence bleaching method called pixel-wise photobleaching profile evolution analysis (3PEA) that extends the strength of FRAP in identifying slowly moving or immobilized particles to include fast translocations and transient binding events as well. 3PEA exploits the inherent time structure of confocal images caused by the sequential nature of the pixel-by-pixel bleaching and imaging process. Protein mobility parameters are obtained by evaluating particle translocations with millisecond time resolution during the acquisition of a single-image frame within less than 1 s. With this method, we were able to quantify the transient binding of the GFP-tagged chromatin remodelers Snf2H and Snf2L. In addition, the naturally occurring splice variant Snf2L+13 was included in the analysis. In Snf2L+13, the exon 13 disrupts the ATPase cassette of Snf2L, which makes the protein inactive. Because Snf2L+13 was found in the same complexes as Snf2L, it was proposed to function as a dominant-negative variant (25). As a reference for proteins that do not interact with chromatin, the isolated GFP/RFP domain and a GFP pentamer (GFP₅) were used. Our 3PEA analysis of Snf2H and Snf2L revealed that transient binding interactions occur with an average residence time below 2 ms, and are thus well separated from the rare long-lived interactions of several seconds to minutes. These results strongly support the view that Snf2H and Snf2L do not translocate nucleosomes during most of their chromatin interaction events in G1 phase because the <2-ms residence time is too short for repositioning a nucleosome.

Theory

Principle of 3PEA. The principle of 3PEA is illustrated in Fig. 1*A* and Movies S1, S2, and S3. In confocal laser scanning microscopy, the individual volume elements (voxels) of a sample are sequentially illuminated in a raster scan process. Thus, every image pixel is acquired at a unique time point. This applies also for the bleach process in FRAP experiments, which occurs in the same pixel-by-pixel manner as the subsequent image acquisition. The only difference is that the excitation laser intensity is largely increased within the bleach region (Fig. 1*A*, red arrows). In the current state-of-the-art FRAP analysis, it is ignored that the CLSM acquires and bleaches images in a sequential manner. Instead, the integrated intensity in the bleach spot or the intensity profile is analyzed over time (9, 10, 15, 26), starting with the first postbleach image shown at the bottom of Fig. 1*A*. Thus, all information on particle mobility during the bleach process is lost. Likewise, translocations that occur during the acquisition time of an image frame, which is around 100 ms per image for the microscope used here, are not resolved. This leads to a relatively low temporal resolution and precludes measurements of faster processes. However, the information on translocations on the millisecond time scale is present in the pixel intensity profile of the bleach frame. This is depicted schematically for particles with high or low mobility in Fig. 1*A*. The 3PEA approach introduced here explicitly calculates and fits the spatiotemporal intensity distribution generated by the sequential bleach process. It can describe the subsequently acquired postbleach images in the same manner. This is shown in Fig. 1*B* for the calculated time evolution of intensity profiles for particles with different diffusion coefficients during and after the bleach process. Moreover, effective translocation probability distributions can be derived without assumptions about the underlying microscopic translocation process. In the following, the theory for the 3PEA method is developed to extract the encoded mobility information. The approach is then applied to dissect the transient binding of the ISWI-type chromatin remodelers Snf2H, Snf2L, and Snf2L+13.

3PEA for Diffusion Processes. The theoretical framework of the 3PEA method is derived here for homogeneous protein distributions. This assumption is valid for all proteins used in this study because they exhibited little spatial variation in their steady-state distribution. For heterogeneous distributions, the intensity profile for the analysis needs to be corrected by subtracting the prebleach distribution. This correction is similar to the well-established procedure for removing immobile protein fractions in RICS (27), and its applicability for 3PEA was confirmed in the analysis of cells exhibiting more heterogeneous chromatin remodeler distributions. The temporal distance between the acquisition of two pixels at (x_0, y_0) and (x_1, y_1) of a CLSM image depends on their spatial coordinates (27) and can be written as

$$\Delta t_{\text{pixel}} = \frac{x_1 - x_0}{s}\tau_{\text{p}} + \frac{y_1 - y_0}{s}\tau_{\text{l}}. \qquad [1]$$

Here, τ_{p} denotes the time between the acquisition of two adjacent pixels within the same line, τ_{l} is the time between the acquisition of two adjacent pixels in successive lines, x and y are the pixel coordinates, and s is the pixel size. If a particle is bleached in a volume element around position (x_0, y_0, z_0), the probability $P_{\text{diff}}(\vec{x}_0, \vec{x}_1, \Delta t)$ that it translocates to position (x_1, y_1, z_1) during the time interval Δt can be expressed according to a

specific model that describes the particle mobility. For pure diffusion, this propagator is given by

$$P_{\text{diff}}(\vec{x}_0, \vec{x}_1, \Delta t) = \frac{1}{(4\pi D \Delta t)^{3/2}} \exp\left(-\frac{(x_1 - x_0)^2 + (y_1 - y_0)^2 + (z_1 - z_0)^2}{4D\Delta t}\right),$$ [2]

with D being the diffusion coefficient of the particle of interest. The point spread function (PSF) of a confocal microscope for detecting a fluorescent particle can be approximated by 3D-Gaussian geometry:

$$PSF(\vec{x}, \vec{x}') = \exp\left(-2\frac{(x' - x)^2 + (y' - y)^2}{w_0^2} - 2\frac{(z' - z)^2}{z_0^2}\right).$$ [3]

Here, w_0 and z_0 are the lateral and axial beam waists, respectively. The PSF is defined in its general form (i.e., as the product of the illumination and detection PSF). The theoretical intensity distribution for a FRAP series acquired with the CLSM (Fig. 1B) is obtained based on the calculation of the amount of particles that were bleached within a volume element around $\vec{x}_i$ and show up in $\vec{x}_1$ when the intensity in the latter position is measured. The loss in fluorescence intensity arising from these bleached particles is proportional to $N_{\vec{x}_i \to x_1}^{\text{r2c}} = N_{\text{bleach}}(\vec{x}_i)P_{\vec{x}_i \to x_1}^{\text{r2c}}$ and is given by Eq. 4:

$$N_{\vec{x}_i \to x_1}^{\text{r2c}} = \frac{N_{\text{bleach}}}{V_{\text{eff}}}(\vec{x}_i) \int_{-\infty}^{\infty} dx' \int_{-\infty}^{\infty} dy' \int_{-\infty}^{\infty} dz' \ PSF(\vec{x}', \vec{x}_1)$$

$$\times \int_{x_i - r_x}^{x_i + r_x} dx \int_{y_i - r_y}^{y_i + r_y} dy \int_{z_i - r_z}^{z_i + r_z} dz \ P_{\text{diff}}(\vec{x}, \vec{x}', \Delta t)$$

$$= \frac{N_{\text{bleach}}(\vec{x}_i)}{8} \Phi\left(x_i - x_1, r_x, \sqrt{\frac{w_0^2}{2} + d^2}\right)$$

$$\times \Phi\left(y_i - y_1, r_y, \sqrt{\frac{w_0^2}{2} + d^2}\right) \Phi\left(z_i - z_1, r_z, \sqrt{\frac{z_0^2}{2} + d^2}\right).$$ [4]

Here, $\Phi(x, r, w) = \text{erf}\left(\frac{x+r}{w}\right) - \text{erf}\left(\frac{x-r}{w}\right)$; $d^2 = 4D\Delta t_{\text{pixel}}$ is the mean squared displacement (MSD) of the particles; $N_{\text{bleach}}(\vec{x}_i)$ is the number of particles bleached in $\vec{x}_i$ (Eq. 5); $V_{\text{eff}} = (\pi/2)^{3/2} w_0^2 z_0$ is the effective PSF volume; and r_x, r_y, and r_z are the edge lengths of the volume element considered (Fig. S1A). To obtain the intensity profiles in the bleach and postbleach frames based on Eq. 4, the amount of particles that become bleached in each volume element of the bleach region has to be known. This value depends on the shape of the PSF that extends the bleach process beyond its center position to neighboring areas. In addition, the translocation of bleached particles during the bleach process has to be accounted for. Thus, even before the illumination beam has reached a voxel of interest, this voxel might contain previously bleached particles. Because the initial number of fluorescent particles varies from voxel to voxel, different numbers of particles become newly bleached in each volume element, even in case of identical illumination intensity. The following recursive relation yields the particles that become bleached in a cuboid volume element around $\vec{x}$ at time t when the focus is located at $\vec{x}_0$:

$$N_{\text{bleach}}(\vec{x}, t) = P_{\text{bleach}}(\vec{x}, \vec{x}_0)$$

$$\times \left(\langle N_{\text{cube}}\rangle - \sum_{t_i < t} \sum_{\vec{x}' \in \text{PSF}_i} N_{\text{bleach}}(\vec{x}', t_i) P_{x' \to x}^{\text{r2r}}(\vec{x}', \vec{x}, t - t_i)\right).$$ [5]

In Eq. 5, $P_{\text{bleach}}(\vec{x}, \vec{x}_0)$ denotes the bleach depth at $\vec{x}$, $\langle N_{\text{cube}}\rangle = cV_{\text{cube}}$ is the average particle number within a cuboid volume element, and P^{r2r} is the translocation probability between two volume elements (SI Text and Fig. S1A). For the first bleach event, the number of bleached particles is determined solely by the bleach depth, which, in turn, depends on the bleach PSF of the microscope (SI Text). For subsequent bleach events, Eq. 5 corrects for the number of bleached particles that are already present in a volume element before the center of the illumination beam has reached it. Accordingly, t_i represents all time points at which bleaching occurred before the center of the illumination beam arrives at position $\vec{x}$, and PSF$_i$ comprises the volume elements that were bleached at time point t_i. If more than one bleach frame is used, the bleach events within previous bleach frames are also included. From Eqs. 4 and 5, the intensity profile for the bleach and postbleach frames is obtained by

$$I(\vec{x}, t) = \varepsilon\left(\langle N\rangle - \sum_{t_i < t} \sum_{\vec{x}' \in \text{PSF}_i} N_{\text{bleach}}(\vec{x}', t_i) P_{x' \to x}^{\text{r2c}}(\vec{x}', \vec{x}, t - t_i)\right).$$ [6]

Here, $\langle N\rangle$ is the average particle number within the focal volume, and ε is the visibility of the molecules (i.e., the amount of detected signal per molecule). The maximum signal that can be obtained is $I_{\text{max}} = \varepsilon\langle N\rangle$. This value is reduced if bleaching has already occurred during the preceding raster scan. With the knowledge of the microscope parameters used in the experiment (pixel time τ_p, line time τ_l, frame time τ_f, and beam waists w_0 and w_b), the expression in Eq. 6 can readily be applied to fit intensity profiles and to determine mobility parameters. As outlined in the following section and described in further detail in SI Text, this general theoretical framework can be used to account for anomalous diffusion or to include binding events explicitly.

3PEA for Reaction-Diffusion Processes. If 3PEA is applied to reaction-diffusion processes, the propagator for pure diffusion given in Eq. 2 is replaced by an expression that also accounts for binding interactions. The probability distribution for a particle's residence time t_{res} at a given position in the presence of binding reactions with pseudoassociation rate k_{on}^* (including the concentration of binding sites), and dissociation rate k_{off} is

$$P_{\text{bound}}(t_{\text{res}}) = F_{\text{eq}}\delta(t_{\text{res}}) + C_{\text{eq}}k_{\text{off}}e^{-k_{\text{off}}t_{\text{res}}}$$

$$= \frac{k_{\text{off}}}{k_{\text{on}}^* + k_{\text{off}}}\left(\delta(t_{\text{res}}) + k_{\text{on}}^* e^{-k_{\text{off}}t_{\text{res}}}\right),$$ [7]

with the free and bound fractions F_{eq} and C_{eq} in steady state. In Eq. 7, the first term is the probability to find a free particle and the second term is the probability to find a particle bound for t_{res}. Accordingly, the following propagator for reaction-diffusion processes can be formulated:

$$P_{\text{reac+diff}}(\vec{x}_0, \vec{x}_1, \Delta t) = F_{\text{eq}} P_{\text{diff}}(\vec{x}_0, \vec{x}_1, \tau_{\text{free}}(\Delta t))$$

$$+ C_{\text{eq}} \int_0^{\Delta t} dt_{\text{res}} \, k_{\text{off}} e^{-k_{\text{off}}t_{\text{res}}} P_{\text{diff}}(\vec{x}_0, \vec{x}_1, \tau_{\text{free}}(\Delta t - t_{\text{res}}))$$

$$+ C_{\text{eq}} e^{-k_{\text{off}}\Delta t} \delta(\vec{x}_0 - \vec{x}_1).$$ [8]
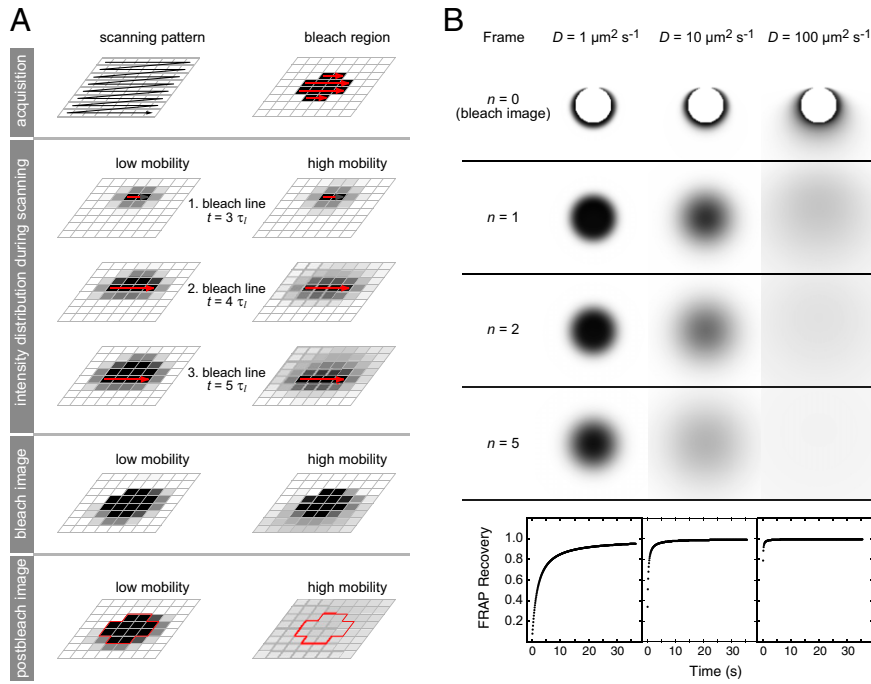
Fig. 1. 3PEA concept. (*A*) A CLSM acquires and bleaches images via a pixel-by-pixel scanning process in a sequential manner. This is not considered in the conventional FRAP analysis. In contrast, 3PEA explicitly calculates and fits the spatiotemporal intensity distribution generated by the sequential bleach process. (*B*) Time evolution of the intensity profiles for particles with different diffusion coefficients during and after the bleach process. The profiles were calculated for a 128×128 image size, a pixel time τ_p of 10 μs, and a line time τ_l of 1 ms. The bleach spot is depicted in white.

Here, $\tau_{\text{free}}(\Delta t)$ is the average time particles have spent in the free state during time Δt if they were in the free state at $t = 0$:

$$\tau_{\text{free}}(\Delta t) = \Delta t \cdot F(\Delta t) = \Delta t \cdot \left(F_{\text{eq}} + C_{\text{eq}}e^{-(k_{\text{on}}^* + k_{\text{off}})\Delta t}\right). \quad [9]$$

In Eq. **9**, $F(t)$ is the free fraction after time t, which can be interpreted as the average fraction of particles in the free state or as the fraction of time an individual particle has spent, on average, in the free state. Per definition, particles are initially free; thus, $F(0) = 1$. For larger time lags Δt, the free fraction decreases to $F(\Delta t \to \infty) = F_{\text{eq}}$ because particles become trapped part of the time. The reaction-diffusion propagator in Eq. **8** can be understood intuitively. The first line represents particles that are initially free and subsequently diffuse for $\tau_{\text{free}}(\Delta t)$. The second line represents particles that are initially bound, dissociate after $t_{\text{res}} < \Delta t$, and diffuse for the rest of the time they spend in the free state [i.e., $\tau_{\text{free}}(\Delta t - t_{\text{res}})$]. The third line represents particles that are initially bound and remain bound for $t_{\text{res}} > \Delta t$. In general, the integral in the second line of Eq. **8** has to be solved numerically. For special cases, such as very fast binding [i.e., $\Delta t >> (k_{\text{on}}^* + k_{\text{off}})^{-1}$] or very slow binding, such as that represented by $P_{\text{bound}}(t_{\text{res}} < \Delta t) \to 0$, Eq. **8** converges to analytical expressions. The scale-dependent behavior of reaction-diffusion processes is illustrated in Fig. S1 *B* and *C*.

The diffusion propagator in Eq. **2** depends only on the product of time and the diffusion coefficient. Thus, if binding events reduce the average time during which a particle is free to diffuse, this can also be accounted for by introducing a time-dependent apparent diffusion coefficient according to Eq. **10**:

$$D_{\text{app}}(\Delta t) = D \cdot F(\Delta t) = D \cdot \left(F_{\text{eq}} + C_{\text{eq}}e^{-(k_{\text{on}}^* + k_{\text{off}})\Delta t}\right)$$
$$= \frac{D}{1 + K_{\text{eq}}^*}\left(1 + K_{\text{eq}}^* e^{-(k_{\text{on}}^* + k_{\text{off}})\Delta t}\right). \quad [10]$$

Here, $K_{\text{eq}}^* = k_{\text{on}}^*/k_{\text{off}}$ is the pseudoequilibrium binding constant that includes the concentration of free binding sites. Eq. **10**

yields the weighted average diffusion coefficient for an ensemble with $F(\Delta t)$ free molecules diffusing with D and the rest of the molecules being bound to immobile obstacles. For large lag times $\Delta t >> (k_{\text{on}}^* + k_{\text{off}})^{-1}$, Eq. **10** converges to the time-independent effective diffusion coefficient $D_{\text{eff}} = D/(1 + K_{\text{eq}}^*)$ introduced previously (28). Further details on the derivation of the above implementation of a reaction-diffusion model into the 3PEA approach are given in *SI Text*.

3PEA for Arbitrary Translocation Processes. To obtain information about particle mobility in a model-independent manner, the translocation probability distribution $P(\Delta x, \Delta t)$ can be directly calculated from the intensity profile by assigning a characteristic spatial and temporal distance with respect to the set of bleach events to every pixel (*SI Text*). In this case, Δx and Δt are averaged values, and thus not exact. Nevertheless, they reflect that each pixel predominantly contains information about a certain range of length and time scales. Based on these characteristic distances, the effective translocation probability can be directly obtained from the pixel intensity via the relation

$$1 - \frac{I(\Delta x, \Delta t)}{\bar{I}} = P(\Delta x, \Delta t). \quad [11]$$

Here, $\bar{I}$ is the average prebleach intensity and $I(\Delta x, \Delta t)$ is the intensity of the respective pixel. With this approach, typical translocation times can be derived for every spatial distance in the experiment and converted into a plot of the mean squared value of Δx vs. the weighted average translocation time. This approach is less accurate than fitting the experimental data to theoretical intensity distributions. However, it requires no assumption on the type of the underlying translocation process and provides valuable diagnostic information on the contribution of diffusion, binding, and spatial constraints to the observed particle mobility.

Time Resolution and Accuracy of 3PEA. The size of the voxels in the calculation of the bleach profiles should be smaller than the PSF and can be chosen according to the desired accuracy and computation speed of the analysis. If the axial extension of the PSF is in the range of the sample thickness, the equations can be simplified because the translocation process is effectively two-dimensional (*SI Text* and Fig. S2).

To save computational time, diffusion occurring during the bleach of line segments or whole bleach lines can be neglected by using a line-shaped bleach PSF (*SI Text*). For typical scan speeds and diffusion coefficients, this simplification is justified. The accuracy of 3PEA with this implementation is still below the time τ_l to acquire one line. Thus, in principle, 3PEA can increase the time resolution of bleach experiments by a factor of τ_l/τ_f, which is larger than two orders of magnitude for typical image sizes of 128×128 or 512×512 pixels. This gain in temporal resolution is due to the modified evaluation scheme and does not depend on the microscope's maximum frame rate. The 3PEA framework derived here is valid for arbitrary shapes of the bleach region and scan trajectories. The latter feature is particularly important if pixel times differ along the scan line, which can be the case for CLSMs (29). As one special case of the theory derived here, point bleach experiments with a fixed beam like those by Koppel et al. (30) can be treated as well by our theoretical framework. This would involve reducing the scan trajectory to a single position and then subdividing the bleach period into multiple pseudobleach frames. In this manner, particle diffusion during the bleach process could be incorporated into the analysis of such experiments. In the limit of infinitesimal voxel size and infinitely large scan speed, the equations presented here converge to the well-known results obtained previously (28, 31) as shown in the *SI Text*.

Results

Mobility Differences Between Snf2H, GFP, RFP, and GFP$_5$ Measured by 3PEA. The mobility of the chromatin remodeler Snf2H-GFP and free RFP were simultaneously measured in living human U2OS cells (Fig. S3) by analyzing only the bleach frame containing a circular (Fig. 2A) or rectangular (Fig. S4A) bleach region. For comparison, exemplary theoretical intensity profiles for different diffusion coefficients and scan speeds were calculated (Fig. 2B and Fig. S4B). As expected, the bleach corona gets broader with increasing diffusion coefficient and decreasing scan speed. From inspection of Fig. 2 and Fig. S4, it is apparent that the key features of the experimental data are reproduced in the calculated profiles. Snf2H-GFP displayed features of the profiles calculated for both $D = 1$ and $10 \ \mu m^2 \cdot s^{-1}$, respectively, whereas the broader corona of free RFP fitted better to the profile for $D = 10 \ \mu m^2 \cdot s^{-1}$. This difference is expected because Snf2H-GFP, as opposed to free RFP, interacts transiently with chromatin, and is thus slowed down (4).

Due to the raster scan process, the bleach coronas are asymmetrical: Along the "fast" horizontal axis, pixels are separated by the short pixel time only, whereas along the "slow" vertical axis, they are separated by the much larger line time, resulting in different shapes of the respective line sections. This is shown in Fig. 3A for experimental bleach profiles from U2OS cells expressing Snf2H-GFP or the GFP, RFP, and GFP$_5$ references. As described above in the context of Eq. **11**, one can assign a characteristic spatial and temporal distance from the bleach region to each image pixel. The corresponding distributions are shown in Fig. 3B, and were used to calculate the effective experimental translocation probability distributions for the different proteins in a model-independent manner (Fig. 3C, experimental maps). The slower Snf2H-GFP displayed a distribution that is elongated along the time axis and shortened along the spatial axis compared with the distributions for GFP and RFP. This reflects that Snf2H-GFP requires more time to translocate a given distance than GFP/RFP
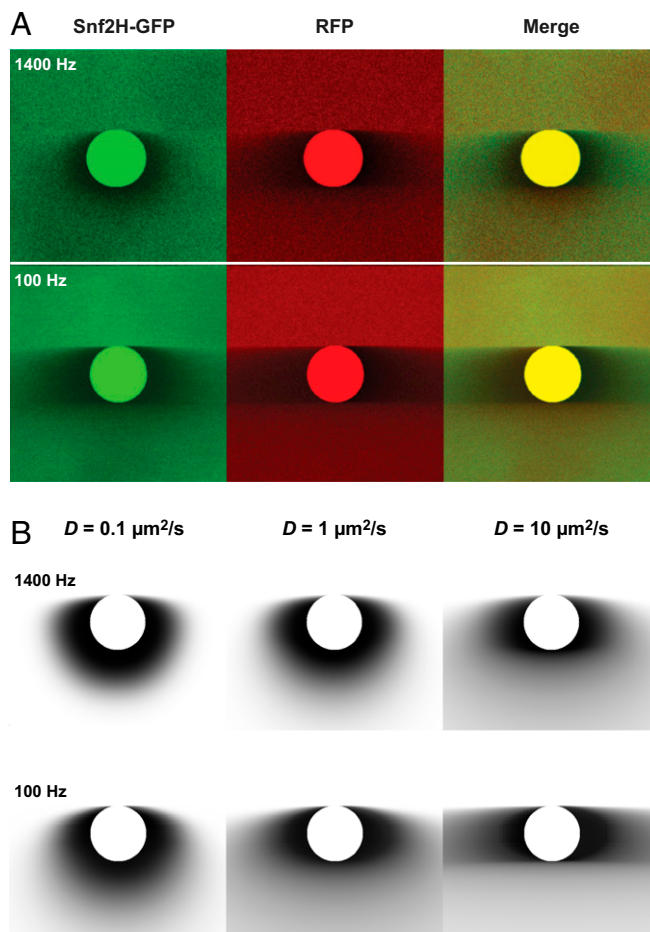
Fig. 2. Experimental implementation of 3PEA. (*A*) Mobilities of Snf2H-GFP and RFP in a U2OS cell line measured in a 3PEA experiment with the indicated scan speeds for raster scanning and a circular bleach region with a diameter of 1 μm. In the merge images, the less mobile protein can be readily identified by visual inspection of the predominant color in the area adjacent to the bleach region (Snf2H-GFP in green). (*B*) Theoretical bleach profiles for different diffusion coefficients calculated for the parameters used in the experiments.

or GFP$_5$, and that fewer molecules reach more distant pixels within the frame time τ_f. The measured translocation probability distributions can readily be evaluated by visual inspection and compared with exemplary theoretical maps for pure diffusion or reaction-diffusion processes with the parameters determined by the profile-fitting analysis described in the next section (diffusion model and reaction-diffusion model in Fig. 3C). It is noted that the reaction-diffusion processes with very small residence times exhibit larger translocation probabilities for short spatial distances (Fig. 3C). A straightforward way to analyze these types of maps is plotting the squared characteristic spatial translocations against the weighted averages along the time axis as shown for GFP and Snf2H (Fig. 3D). The translocation times grow with increasing spatial distance for both GFP and Snf2H. Due to its lower mobility, translocation times for Snf2H are larger than those for GFP. It is noted that both proteins do not show scale-dependent mobility in this type of analysis, which would result in biphasic behavior of the curves.

Diffusion Coefficients for Chromatin Remodelers and Reference Proteins. To obtain quantitative mobility information from 3PEA experiments, the intensity distributions of Snf2H-GFP, GFP-Snf2L,
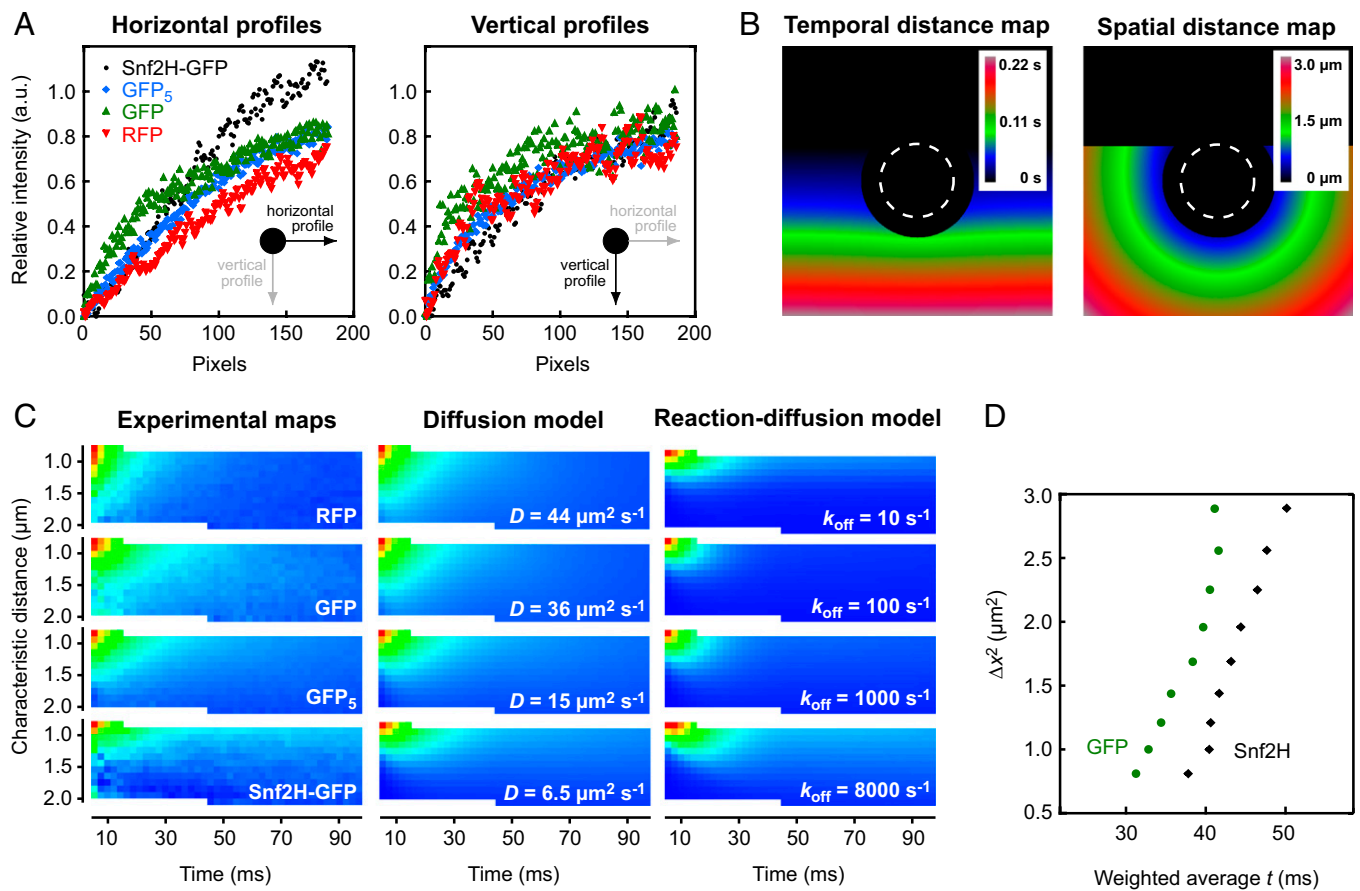
Fig. 3. Translocation probabilities for Snf2H-GFP, GFP, RFP, and GFP$_5$. (*A*) Horizontal and vertical profiles around the bleach spot differ due to the asymmetry introduced by the raster scan process. Different protein mobility leads to different profiles. a.u., arbitrary units. (*B*) Each pixel has a defined characteristic spatial and temporal distance from the set of bleach events. Pixels at the bottom are acquired later than pixels in the center of the image. (*C*) Characteristic spatial and temporal distances can be used to derive the effective translocation probability, $P(\Delta x, \Delta t)$. This distribution depends on the protein mobility as shown for the experimental bleach profiles of the different proteins used here. Theoretical profiles show similar probability distributions. (*D*) Based on the translocation probabilities, the characteristic translocation time can be calculated as the weighted average along the time axis. The resulting diagnostic plots visualize the particle's mobility on different length scales.

GFP-Snf2L+13, GFP, RFP, and GFP$_5$ were fitted against theoretical profiles (Fig. 4, Fig. S5, and Table 1). The best fit was determined based on the sum of squared residuals (SSR). This value is a measure of the fit quality and has a minimum for the profile with the largest similarity to the experimental data. To determine the diffusion coefficient of the mobile pool, only pixels with a distance of at least 400 nm from the bleach spot were evaluated. Pixels adjacent to the bleach spot that contain information about immobile proteins were ignored for simplicity. 3PEA yielded effective diffusion coefficients of 5–7 $\mu m^2 \cdot s^{-1}$ for Snf2H and Snf2L that were clearly lower than that of the similar-sized GFP$_5$ with $D = 15 \pm 2$ $\mu m^2 \cdot s^{-1}$ (Fig. 4*A*, Fig. S5, and Table 1). Thus, the effective diffusion coefficients measured for the active ISWI ATPases include a contribution from transient binding of the protein to chromatin. It is noted that identical values of D_{eff} were obtained for Snf2L and the inactive Snf2L+13 variant (Table 1), which demonstrates that the duration of these binding interactions is not affected by the remodeler's ATP hydrolysis activity. The conventional FRAP analysis conducted using the postbleach images of the same dataset yielded $D_{eff} = 0.7$ $\mu m^2 \cdot s^{-1}$ (with a confidence interval of $D_{eff} = 0.5$–2.0 $\mu m^2 \cdot s^{-1}$) for Snf2H-GFP but failed to determine the diffusion coefficient for RFP (Fig. 4*B*). Because we used a larger image size, and thus a lower frame rate compared with our previous study (4), conventional FRAP yielded a considerably lower value for Snf2H-

GFP. This deviation can be corrected by using a broader bleach profile as initial condition for the fit (17, 32). For the inert GFP and RFP reference protein domains, 3PEA yielded averaged values of $D = 40 \pm 4$ $\mu m^2 \cdot s^{-1}$ in excellent agreement with previous studies (32, 33).

Determination of the Dissociation Rate Constant for Snf2H, Snf2L, and Snf2L+13. The effective diffusion coefficients determined for Snf2H, Snf2L, and Snf2L+13 in the previous section contain binding contributions from interactions with chromatin. This is apparent from the comparison with the diffusion coefficients obtained for inert proteins of comparable size, such as GFP$_5$ (Table 1), or from diffusion coefficient measurements of these proteins in the cytosol by FCS (4). Reliable dissection of binding times on chromatin from this reduction of the apparent diffusion coefficient is essential to evaluate if chromatin remodeler activity is present. However, our previously used approach faced technical limitations (4). On the one hand, a relatively short residence time for transient binding needed to be determined more exactly than was possible by conventional FRAP with a time resolution of roughly 100 ms. On the other hand, a protein fraction potentially immobilized on the time scale of more than 10 ms would be hardly accessible to FCS measurements. This is due to contributions to this part of the autocorrelation curve that arise from unintentional photobleaching and the presence of a second com-

Erdel and Rippe
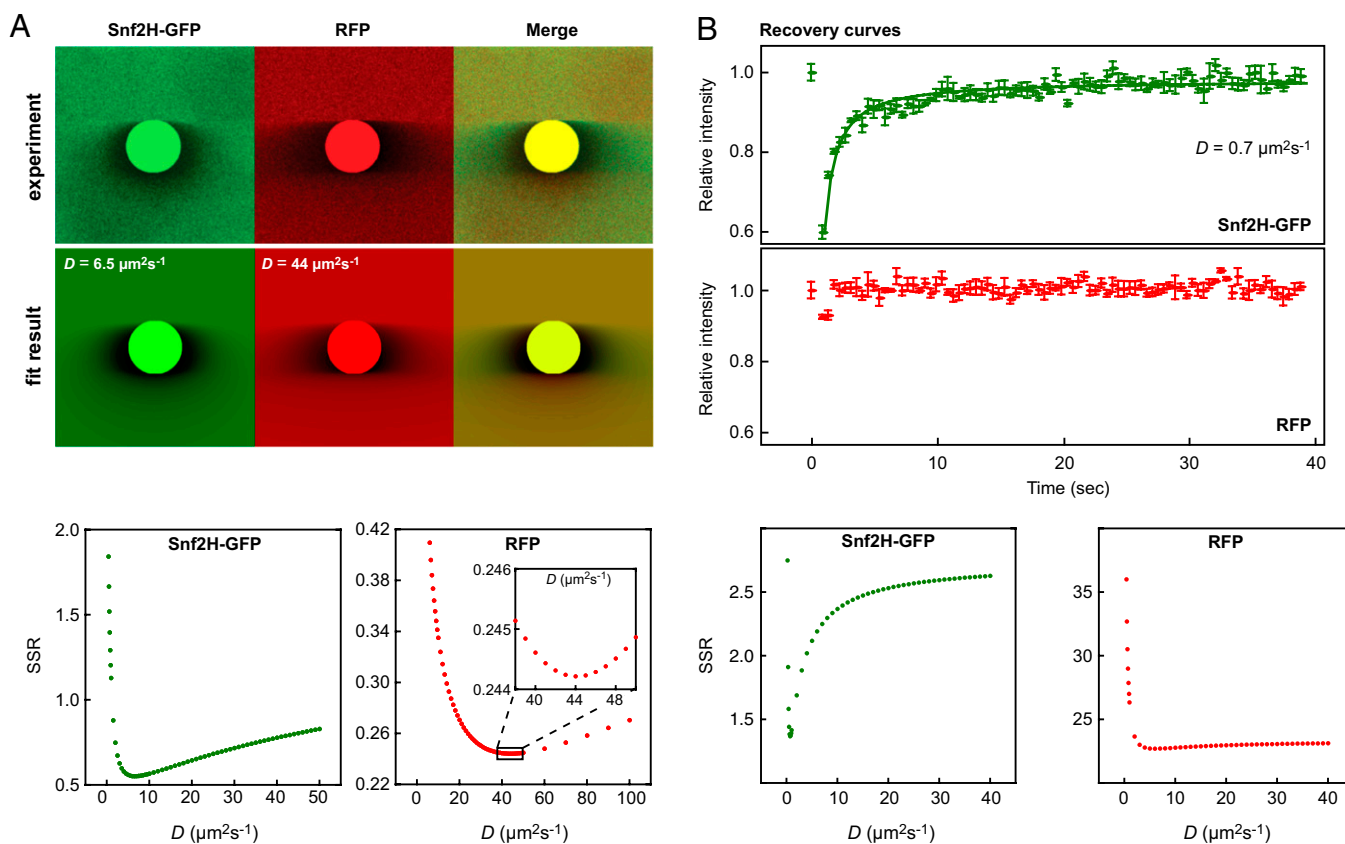
Fig. 4. Diffusion coefficients measured by 3PEA and conventional FRAP. (*A*) Experimental bleach profiles for the scan speed of 1,400 Hz shown in Fig. 2 were fitted to a library of theoretical 3PEA profiles calculated for different diffusion coefficients, yielding $D = 6.5 \pm 1.0\ \mu m^2 \cdot s^{-1}$ for Snf2H-GFP and $D = 44 \pm 3\ \mu m^2 \cdot s^{-1}$ for free RFP. The fit optimum was determined based on the SSR, which has a minimum for the theoretical profile with the largest similarity to the experimental one. The value for Snf2H-GFP was better defined than the result for RFP as evident from the narrower minimum in the SSR plot. (*B*) Conventional FRAP analysis of the same experiment yielded $D = 0.7\ \mu m^2 \cdot s^{-1}$ for Snf2H-GFP and failed to determine the diffusion coefficient for RFP.
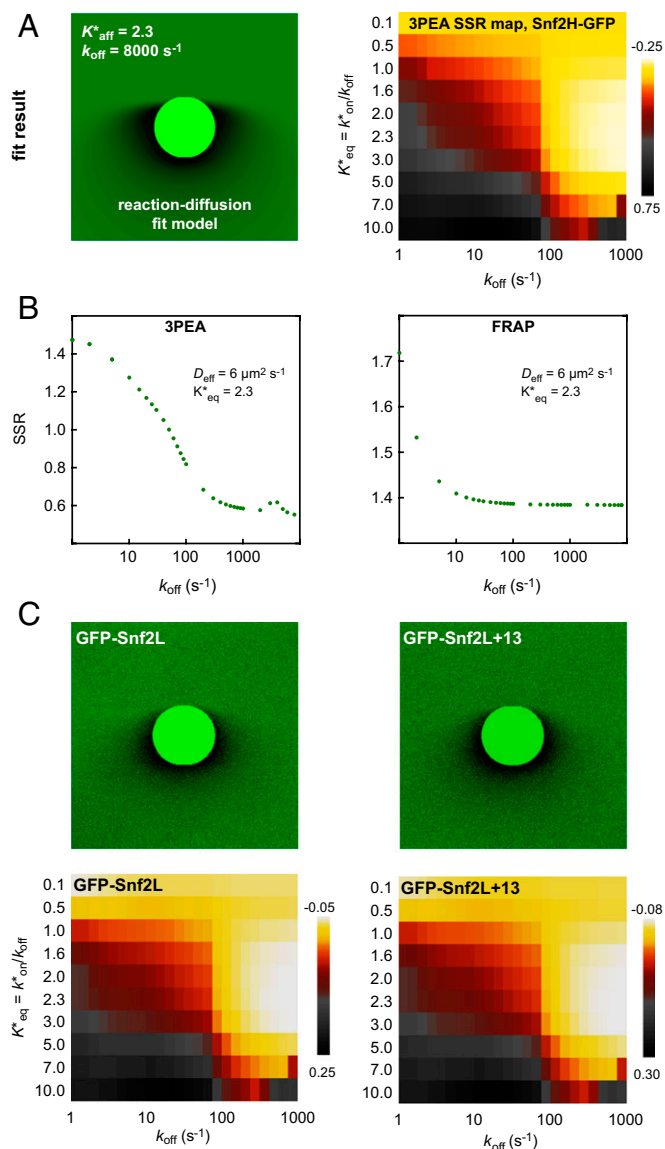
ponent in the correlation function due to chromatin dynamics on the 10- to 500-ms time scale (4, 15). The latter can be directly measured by single-particle tracking of chromatin loci (34, 35). As illustrated in Fig. S6*B* and consistent with previous findings (36), there is no simple way to retrieve the contribution of chromatin binding from the FCS curves [i.e., to decide if a factor interacts with an immobile (chromatin) substrate or if a bound fraction jiggles around an equilibrium position together with the chromatin fiber]. These problems can be overcome when applying the theoretical 3PEA framework for reaction-diffusion processes derived above. The bleach profiles for Snf2H-GFP, GFP-Snf2L, and GFP-Snf2L+13 were fitted with different val-

ues for the dissociation rate constant k_{off} (Fig. 5). Different pseudoequilibrium binding constants were used, including the values of $K^*_{eq} = 2.3$ and $K^*_{eq} = 1.0$ determined previously (4). For Snf2H, good fits to the experimental data were obtained for $k_{off} > 500\ s^{-1}$ as judged from the resulting SSR plots (Fig. 5 *A* and *B*). In contrast, conventional fitting of the FRAP recovery curve could only retrieve a limit of $k_{off} > 10\ s^{-1}$, which is expected based on the 100-ms frame time (Fig. 5*B*). Thus, 3PEA is sensitive to a much wider range of dissociation rates than FRAP, which is in line with the theoretical expectations (*SI Text*), and the finding that fast reaction-diffusion processes can be better studied on small scales (36). For Snf2L and the inactive isoform Snf2L+13, very similar SSR landscapes were obtained with good fits for $k_{off} > 600\ s^{-1}$ (Fig. 5*C*). These results indicate that transient chromatin interactions of Snf2H, Snf2L, and Snf2L+13 occur in a very similar manner. Because Snf2L+13 cannot hydrolyze ATP, the transient binding on the <2-ms scale does not depend on chromatin remodeling activity but, instead, reflects the unproductive interaction with potential substrates. This is consistent with the rate constants on the time scale of seconds measured for chromatin remodeling in vitro (21–24). Because the majority of interactions between remodelers and chromatin occur on the millisecond time scale, remodeling events seem to be rare. Taken together, our 3PEA results point to very short residence times for Snf2H, Snf2L, and Snf2L+13 on chromatin of less than 2 ms, in agreement with dwell times of ~1.4 ms derived from the difference of FCS measurements in the nucleus (τ ~2.0 ms) and the cytoplasm (τ ~0.6 ms) (4). Thus, 3PEA was able to resolve the sampling times for transient interactions of the three remod-

Table 1. Mobility and interaction parameters of ISWI remodelers and GFP/RFP references

Protein	D_{eff}, $\mu m^2 \cdot s^{-1}$	K^*_{eq}	k_{off}, s^{-1}	Method
Snf2H-GFP	6.5 ± 1.0	2.1 ± 0.5	>500	3PEA
GFP-Snf2L	5.5 ± 1.5	2.6 ± 1.0	>600	
GFP-Snf2L+13	5.5 ± 1.5	2.6 ± 1.0	>600	
GFP$_5$	15 ± 2	—	—	
RFP	44 ± 3			
GFP	36 ± 5			
GFP	44 ± 4	—	—	FCS†

†This value was determined using TetraSpeck beads as a reference for which $D = 4.4\ \mu m^2 \cdot s^{-1}$ has been determined by dual-focus FCS and dynamic light scattering (47). This is consistent with the theoretical diffusion coefficient for a sphere with a diameter of 100 nm.

Fig. 5. Dissociation constants measured by 3PEA. (*A*) The bleach profile for Snf2H-GFP was fitted against a library with different dissociation rates. The calculated profile that yielded the best fit and the logarithmic SSR map for different dissociation rates and pseudoequilibrium binding constants are shown. (*B*) The SSR plot for Snf2H-GFP displayed a global minimum at $K^*_{eq} = 2.3$ and $k_{off} > 500$ s^{-1}, corresponding to residence times of less than 2 ms. (*C*) The same analysis was conducted for GFP-Snf2L and GFP-Snf2L+13, yielding very similar SSR maps and best fits for $K^*_{eq} = 2.6$ and rate constants $k_{off} > 600$ s^{-1}.

elers in a time regime that previously was only accessible by FCS. Furthermore, the 3PEA results show that there is no significant fraction of Snf2H molecules binding to chromatin for 10–500 ms, which could not be excluded by the previously used combination of FRAP and FCS.

Discussion

The cell stably maintains its genome and, at the same time, is able to switch reversibly between different functional states. This dichotomy between stability and plasticity is reflected by the dynamic organization of the genome into distinct patterns of chromatin states that can be reorganized in terms of their spatial conformation, protein, and RNA composition as well as by posttranslational modifications of histone and DNA components. Although the vast majority of measurements in living cells

were conducted on the time scale of seconds to hours (16), it is emerging that many processes that affect chromatin function occur in the subsecond time regime. This is true for spontaneous chromatin conformation changes in the nucleus (34, 35) as well as for the occurrence of functionally very different interactions of protein factors with chromatin (1–3). The analysis of ISWI-type chromatin remodeler mobility in living cells conducted here clearly revealed transient binding to chromatin as reflected by the value of the effective diffusion coefficient in comparison to that of a GFP pentamer, which has a similar molecular weight (Table 1). Maximum residence times of 2 ms were found for Snf2H, Snf2L, and the inactive splice variant Snf2L+13. In conjunction with the results from our previous FCS and FRAP analysis (4), the following picture emerges: ISWI chromatin remodelers continuously sample nucleosomes via binding interactions that do not involve ATP hydrolysis and, on average, last only for 1–2 ms. Within this time, it can be tested whether a given nucleosome carries additional signals that would mark it to be translocated. Because any subsequent conformational changes and ATP hydrolysis steps would occur only for a fraction of a few percent of binding events during the G1 phase of the cell cycle, these cannot be further dissected. However, when investigating Snf2H or Snf2L at sites of DNA replication and repair, it is clear that the average chromatin interaction time is at least 30 s at these loci with high remodeler activity (4, 5). This is consistent with the catalytic reaction rates from in vitro experiments that yield a similar time needed for ATP hydrolysis and translocation reactions (21–24). In addition, our model fits well to studies with ISWI mutant *Drosophila* showing that only a small subset of nucleosomes is affected by ISWI activity, arguing for rather rarely occurring translocation events (26).

The additional insight into the dynamics of remodeler–chromatin interactions described above could only be obtained by overcoming various limitations of conventional FRAP with our 3PEA method. 3PEA evaluates the millisecond time information inherent to the pixel-by-pixel bleaching and detection process of a conventional CLSM and the resulting profile of the bleach frame. The power of the method was demonstrated here in a mobility analysis of the transient ISWI chromatin binders in comparison to the inert GFP/RFP using standard CLSM hardware. Diffusion coefficients could be obtained robustly by solely analyzing the bleach frame acquired within less than 1 s of measurement time. Notably, the time scale of 2–500 ms relevant for characterizing the fast transient binding interactions of Snf2H, Snf2L, and Snf2L+13 with chromatin could be characterized. This time scale is not accessible by conventional FRAP because of the roughly two orders of magnitude lower time resolution, and FCS measurements are not suited to quantify chromatin interactions that exceed ~10 ms of residence time due to slow fluctuations on this time scale arising from chromatin dynamics. It is noted that the time resolution for FRAP can also be improved to reach the 1-ms time regime if a dedicated spot bleach instrument with a fixed beam position is used, as done in the early applications of photobleaching to measurements of diffusion (e.g., 30). Spot bleach experiments can be regarded as a special case of the general 3PEA theory developed here for scanned beams. Interpretation of such experiments within our theoretical framework has the advantage that diffusion of particles during the bleach process can be accounted for, which is relevant for the longer bleach periods that might be required to obtain sufficient bleach depths. However, compared to 3PEA with a CLSM setup as implemented here, spot bleach experiments do not yield mobility information on multiple length scales, which is advantageous for the characterization of scale-dependent processes, such as reaction-diffusion processes or anomalous diffusion (*SI Text*).

The averaged 3PEA values of $D = 40 \pm 4$ μm^2·s^{-1} for the inert GFP/RFP reference protein domains obtained here are in ex-

cellent agreement with the values of $D = 41 \pm 4 \; \mu m^2 \cdot s^{-1}$ and $D = 41 \pm 6 \; \mu m^2 \cdot s^{-1}$ from two other studies (32, 33). This demonstrates that the 3PEA method provides accurate values for the determination of D even for highly mobile particles. In the previous studies, a GFP variant was photoactivated in half of the cell nucleus and traced so that faster particles could be measured more accurately at the expense of a reduced spatial resolution (33) or the bleach corona was accounted for with a Gaussian distribution (32). The small difference between similar-sized GFP and RFP might be due to their different photophysical properties (37, 38). Our GFP/RFP and GFP$_5$ values were somewhat larger than those from previous FCS measurements for which diffusion coefficients of 20–30 $\mu m^2 \cdot s^{-1}$ and 8–10 $\mu m^2 \cdot s^{-1}$ were reported (19, 39). This is consistent with the finding that single-focus FCS generally underestimates diffusion coefficients due to deviations of the focal volume from the Gaussian geometry (40), leading to inaccuracies as evident from the comparison of single- and double-focus FCS measurements of small inorganic dyes (40, 41). In our previous study, we used Alexa 488 maleimide with a too small literature value of $D = 210 \; \mu m^2 \cdot s^{-1}$ (42) as a reference. From calibration measurements with well-defined 100-nm size fluorescent latex beads (Fig. S6A and Table 1), we conclude that our previous single-focus FCS analysis of ISWI remodelers (4) underestimated the diffusion coefficients by a factor of roughly 1.5. This leads to a corrected value of $D_{eff} = 20 \pm 2 \; \mu m^2 \cdot s^{-1}$ for Snf2H-GFP in the cytoplasm and of $D_{eff} = 5.9 \pm 0.6 \; \mu m^2 \cdot s^{-1}$ in the nucleus. The latter value is again in good agreement with the 3PEA result of $D_{eff} = 6.5 \pm 1.0 \; \mu m^2 \cdot s^{-1}$. Thus, consistent results are obtained with FCS measurements that use reference values from well-characterized fluorescent particles calibrated by a dual-focus setup and dynamic light scattering (40). The 3PEA method does not require an additional reference with a known diffusion coefficient because it calculates the mobility from the known distance between pixels. This is conceptually similar to correlation methods measuring at spatially separated positions, such as dual-focus FCS, RICS, or pair correlation analysis (14, 27, 41).

A 3PEA measurement can be conducted within 1 s or less, and the method opens up several new approaches for single-cell protein interaction analyses via evaluating protein dynamics in living cells:

i) Changes in intracellular protein mobility of highly dynamic cellular states that are adopted in response to external stimuli, such as drug treatment, mechanical stress, or DNA damage, can be detected with a time resolution of 1 s.

ii) Automated high-throughput FRAP experiments will be largely facilitated. This would both improve the reliable detection of differences in intracellular protein mobility and provide a new readout in RNAi screening experiments for systems biology studies of protein networks (43).

iii) Acquiring protein mobility maps with a resolution on the micrometer scale becomes feasible by sequentially probing multiple locations in the same cell by 3PEA. In such experiments, reversible photoswitching of a suitable fluorophore to a dark state can be used instead of bleaching (44–46), thus enabling hundreds of 3PEA cycles per cell without depleting the pool of fluorescent particles.

iv) Precise dissection of the binding and diffusion behavior exhibited by a protein of interest can be achieved by applying 3PEA to additional images of the postbleach series to improve the robustness and the resolution of dynamics on different time scales.

v) Similar to the pair correlation analysis introduced by Gratton and coworkers (14), it would be possible to measure anisotropic diffusion of molecules in living cells by 3PEA. This would involve evaluating the bleach profile at different distances and locations to define areas with increased translocation probabilities and to identify directed transport and/or diffusion barriers.

vi) By combining 3PEA with conventional FRAP analysis for late time points, it is straightforward to cover a binding time range from ~2 ms to minutes and to quantify both highly mobile and immobilized fractions in a single bleach experiment.

In summary, the 3PEA method extracts comprehensive protein mobility information over a large dynamic range at an unprecedented accuracy that is particularly valuable to characterize interactions of protein factors with chromatin. It is anticipated that experiments along the lines described here will also yield valuable information on other factors that need to identify their chromosomal target sites efficiently via transient interactions to maintain or change functional chromatin states.

Materials and Methods

Cell Culture and Plasmids. U2OS cells stably expressing Snf2H-GFP were grown in LabTek chambers (Nalge Nunc) as described previously (4). Transient transfection of pTagRFP-C (Evrogen), pEGFP-N1 (BD Biosciences Clontech), pTagRFP-Snf2H (4), or pEGFP$_5$ (19) was done using the transfection reagent Effectene (Qiagen) according to the manufacturer's protocol.

Microscopy. 3PEA experiments were carried out on a Leica SP5 microscope equipped with an HCX PL APO lambda blue 63× oil immersion objective with an N.A. of 1.4 (Leica). Images were acquired with 512 × 512 pixels in size and a scanning speed of 100 Hz or 1,400 Hz, which corresponds to frame times of roughly 6.5 s or 450 ms, respectively. The diameter of the circular bleach spot was chosen to be 1 μm, and the rectangular region had a height of 2 μm and a width of 0.5 μm. To account for the width of the bleach PSF, a circle diameter of 2 μm was used for the conventional FRAP analysis. For bleaching, an argon laser at 488 nm or a diode-pumped solid-state laser at 561 nm was used, both at a power of ~2 mW in the back aperture of the objective. The experimental profiles for Snf2H-GFP and RFP shown above were averaged over six experiments conducted in three cells. For the other profiles, at least 20 measurements were averaged. FCS experiments were carried out on a Zeiss LSM 710 ConfoCor 3 microscope equipped with a 63× water immersion objective with an N.A. of 1.2 (Zeiss). TetraSpeck 0.1-μm fluorescent microspheres (Invitrogen) were used for calibration of the microscope's PSF.

Calculations and Software Implementation. Integrations were carried out using Maple 12 (Maplesoft). Theoretical intensity profiles were generated using a custom-made program written in C++ running on an HP computer cluster (Hewlett Packard) with 128 cores. Bleach profiles used for fitting were calculated with an image size of 512 × 512 pixels, a pixel size of 7.5 nm, a detection beam waist of 300 nm, and a bleach beam waist of 400 nm (the experimental bleach PSF is shown in Fig. S2). A line-shaped bleach PSF was used (see below), and a binning step of eight pixels in scan direction was performed to accelerate the computation. The calculation of one profile of this type required ~24 h of computation time using one core for the diffusion model, or up to 7 d for the reaction-diffusion model with very large dissociation rates. These calculations need to be made only once for each parameter set and can then be used in tabulated form for the fitting of experimental data to implement the 3PEA approach according to the algorithm depicted in Fig. S7.

Fitting and Error Estimation. The bleach profile around the circular bleach region was used for determining the fit optimum and for the generation of the SSR profile. To this end, a library with calculated intensity profiles was compared with the experimentally acquired one, which reduced the time required for fitting to below 1 min. A similar strategy was reported previously to compare numerical Monte Carlo simulations with FRAP recovery curves (47). The theoretical profiles were scaled to account for varying bleach depths and gain settings of the microscope, according to the formula $I' = I_0 + sI$. Here, I_0 is an offset and s is a scale parameter. Both parameters were adjusted such that the prebleach intensity above the bleach region and the total intensity in the rest of the image corresponded to the experimentally obtained values. The error limits given in the text correspond to the profiles with an SSR that is 0.05% larger than the SSR for the optimum profile. Due to the large number of data points, which correspond to all image pixels outside the bleach region (>200,000 pixels), the statistical confidence within these limits is still higher than 95%. For comparison, the SD between different cells was used, which yielded similar values.

1. Hager GL, McNally JG, Misteli T (2009) Transcription dynamics. *Mol Cell* 35(6):741–753.
2. van Royen ME, Zotter A, Ibrahim SM, Geverts B, Houtsmuller AB (2011) Nuclear proteins: Finding and binding target sites in chromatin. *Chromosome Res* 19(1):83–98.
3. Erdel F, Krug J, Längst G, Rippe K (2011) Targeting chromatin remodelers: Signals and search mechanisms. *Biochim Biophys Acta* 1809(9):497–508.
4. Erdel F, Schubert T, Marth C, Längst G, Rippe K (2010) Human ISWI chromatin-remodeling complexes sample nucleosomes via transient binding reactions and become immobilized at active sites. *Proc Natl Acad Sci USA* 107(46):19873–19878.
5. Erdel F, Rippe K (2011) Binding kinetics of human ISWI chromatin-remodelers to DNA repair sites elucidate their target location mechanism. *Nucleus* 2(2):105–112.
6. Clapier CR, Cairns BR (2009) The biology of chromatin remodeling complexes. *Annu Rev Biochem* 78:273–304.
7. Erdel F, Rippe K (2011) Chromatin remodelling in mammalian cells by ISWI-type complexes—Where, when and why? *FEBS J* 278(19):3608–3618.
8. Erdel F, Müller-Ott K, Baum M, Wachsmuth M, Rippe K (2011) Dissecting chromatin interactions in living cells from protein mobility maps. *Chromosome Res* 19(1):99–115.
9. Houtsmuller AB (2005) Fluorescence recovery after photobleaching: Application to nuclear proteins. *Adv Biochem Eng Biotechnol* 95:177–199.
10. Sprague BL, McNally JG (2005) FRAP analysis of binding: Proper and fitting. *Trends Cell Biol* 15(2):84–91.
11. Elson EL (2011) Fluorescence correlation spectroscopy: Past, present, future. *Biophys J* 101(12):2855–2870.
12. Hebert B, Costantino S, Wiseman PW (2005) Spatiotemporal image correlation spectroscopy (STICS) theory, verification, and application to protein velocity mapping in living CHO cells. *Biophys J* 88(5):3601–3614.
13. Digman MA, et al. (2005) Fluctuation correlation spectroscopy with a laser-scanning microscope: Exploiting the hidden time structure. *Biophys J* 88(5):L33–L36.
14. Hinde E, Cardarelli F, Digman MA, Gratton E (2010) In vivo pair correlation analysis of EGFP intranuclear diffusion reveals DNA-dependent molecular flow. *Proc Natl Acad Sci USA* 107(38):16560–16565.
15. Müller KP, et al. (2009) Multiscale analysis of dynamics and interactions of heterochromatin protein 1 by fluorescence fluctuation microscopy. *Biophys J* 97(11):2876–2885.
16. Wachsmuth M, Caudron-Herger M, Rippe K (2008) Genome organization: Balancing stability and plasticity. *Biochim Biophys Acta* 1783(11):2061–2079.
17. Mueller F, Wach P, McNally JG (2008) Evidence for a common mode of transcription factor interaction with chromatin as revealed by improved quantitative fluorescence recovery after photobleaching. *Biophys J* 94(8):3323–3339.
18. Mueller F, Mazza D, Stasevich TJ, McNally JG (2010) FRAP and kinetic modeling in the analysis of nuclear protein dynamics: What do we really know? *Curr Opin Cell Biol* 22(3):403–411.
19. Pack C, Saito K, Tamura M, Kinjo M (2006) Microenvironment and effect of energy depletion in the nucleus analyzed by mobility of multiple oligomeric EGFPs. *Biophys J* 91(10):3921–3936.
20. Stasevich TJ, et al. (2010) Cross-validating FRAP and FCS to quantify the impact of photobleaching on in vivo binding estimates. *Biophys J* 99(9):3093–3101.
21. He X, Fan HY, Narlikar GJ, Kingston RE (2006) Human ACF1 alters the remodeling strategy of SNF2h. *J Biol Chem* 281(39):28636–28647.
22. Racki LR, et al. (2009) The chromatin remodeller ACF acts as a dimeric motor to space nucleosomes. *Nature* 462(7276):1016–1021.
23. Zhang Y, et al. (2006) DNA translocation and loop formation mechanism of chromatin remodeling by SWI/SNF and RSC. *Mol Cell* 24(4):559–568.
24. Blosser TR, Yang JG, Stone MD, Narlikar GJ, Zhuang X (2009) Dynamics of nucleosome remodelling by individual ACF complexes. *Nature* 462(7276):1022–1027.
25. Barak O, Lazzaro MA, Cooch NS, Picketts DJ, Shiekhattar R (2004) A tissue-specific, naturally occurring human SNF2L variant inactivates chromatin remodeling. *J Biol Chem* 279(43):45130–45138.
26. Sala A, et al. (2011) Genome-wide characterization of chromatin binding and nucleosome spacing activity of the nucleosome remodelling ATPase ISWI. *EMBO J* 30(9):1766–1777.
27. Digman MA, et al. (2005) Measuring fast dynamics in solutions and cells with a laser scanning microscope. *Biophys J* 89(2):1317–1327.
28. Sprague BL, Pego RL, Stavreva DA, McNally JG (2004) Analysis of binding reactions by fluorescence recovery after photobleaching. *Biophys J* 86(6):3473–3495.
29. Gröner N, Capoulade J, Cremer C, Wachsmuth M (2010) Measuring and imaging diffusion with multiple scan speed image correlation spectroscopy. *Opt Express* 18(20):21225–21237.
30. Koppel DE, Axelrod D, Schlessinger J, Elson EL, Webb WW (1976) Dynamics of fluorescence marker concentration as a probe of mobility. *Biophys J* 16(11):1315–1329.
31. Soumpasis DM (1983) Theoretical analysis of fluorescence photobleaching recovery experiments. *Biophys J* 41(1):95–97.
32. Kang M, Day CA, Drake K, Kenworthy AK, DiBenedetto E (2009) A generalization of theory for two-dimensional fluorescence recovery after photobleaching applicable to confocal laser scanning microscopes. *Biophys J* 97(5):1501–1511.
33. Beaudouin J, Mora-Bermúdez F, Klee T, Daigle N, Ellenberg J (2006) Dissecting the contribution of diffusion and interactions to the mobility of nuclear proteins. *Biophys J* 90(6):1878–1894.
34. Levi V, Ruan Q, Plutz M, Belmont AS, Gratton E (2005) Chromatin dynamics in interphase cells revealed by tracking in a two-photon excitation microscope. *Biophys J* 89(6):4275–4285.
35. Jegou T, et al. (2009) Dynamics of telomeres and promyelocytic leukemia nuclear bodies in a telomerase-negative human cell line. *Mol Biol Cell* 20(7):2070–2082.
36. Michelman-Ribeiro A, et al. (2009) Direct measurement of association and dissociation rates of DNA binding in live cells by fluorescence correlation spectroscopy. *Biophys J* 97(1):337–346.
37. Kremers GJ, Hazelwood KL, Murphy CS, Davidson MW, Piston DW (2009) Photoconversion in orange and red fluorescent proteins. *Nat Methods* 6(5):355–358.
38. Mueller F, Morisaki T, Mazza D, McNally JG (2012) Minimizing the impact of photoswitching of fluorescent proteins on FRAP analysis. *Biophys J* 102(7):1656–1665.
39. Hendrix J, Flors C, Dedecker P, Hofkens J, Engelborghs Y (2008) Dark states in monomeric red fluorescent proteins studied by fluorescence correlation and single molecule spectroscopy. *Biophys J* 94(10):4103–4113.
40. Dertinger T, et al. (2007) Two-focus fluorescence correlation spectroscopy: A new tool for accurate and absolute diffusion measurements. *Chemphyschem* 8(3):433–443.
41. Muller CB, et al. (2008) Precise measurement of diffusion by multi-color dual-focus fluorescence correlation spectroscopy. *Europhys Lett* 83(46001):1–5.
42. Swaminathan R, Bicknese S, Periasamy N, Verkman AS (1996) Cytoplasmic viscosity near the cell plasma membrane: translational diffusion of a small fluorescent solute measured by total internal reflection-fluorescence photobleaching recovery. *Biophys J* 71(2):1140–1151.
43. Conrad C, et al. (2011) Micropilot: Automation of fluorescence microscopy-based imaging for systems biology. *Nat Methods* 8(3):246–249.
44. Subach FV, et al. (2010) Red fluorescent protein with reversibly photoswitchable absorbance for photochromic FRET. *Chem Biol* 17(7):745–755.
45. Brakemann T, et al. (2011) A reversibly photoswitchable GFP-like protein with fluorescence excitation decoupled from switching. *Nat Biotechnol* 29(10):942–947.
46. Grotjohann T, et al. (2011) Diffraction-unlimited all-optical imaging and writing with a photochromic GFP. *Nature* 478(7368):204–208.
47. van Royen ME, et al. (2009) Fluorescence recovery after photobleaching (FRAP) to study nuclear protein dynamics in living cells. *Methods Mol Biol* 464:363–385.

Supporting Information

Erdel and Rippe 10.1073/pnas.1209579109

SI Text

Scale-Dependent Behavior of Reaction-Diffusion Processes. Simple diffusion processes can be studied on different length and time scales because the diffusion coefficient is scale-independent for length scales significantly larger than the mean free path and for time scales well above the inverse collision rate. However, this is different for a reaction-diffusion process that exhibits different scale-dependent properties. For the theoretical description given below, it is instructive to consider a reaction-diffusion process as a pseudofirst-order reaction, in which particles exchange between a free state (F) and an immobile complex (C). In biological systems, this scenario reflects the binding of a mobile factor to an essentially immobile substrate with an excess of potential binding sites, such as chromatin in the cell nucleus or the cytoskeleton in the cytosol. The probability to find particles in the free or the bound state depends on the kinetic on and off rates for binding, k_{on} and k_{off}, and obeys the following differential equations:

$$\frac{\partial F}{\partial t} = k_{off}C - k_{on}^{*}F$$
$$\frac{\partial C}{\partial t} = k_{on}^{*}F - k_{off}C, \qquad \text{[S1]}$$

with $F + C = 1$. The parameter k_{on}^{*} is the product of the kinetic on rate and the average concentration of free binding sites. In steady state, the derivatives vanish and the bound and free fractions are given by

$$F_{eq} = \frac{k_{off}}{k_{on}^{*} + k_{off}}, \quad C_{eq} = \frac{k_{on}^{*}}{k_{on}^{*} + k_{off}}. \qquad \text{[S2]}$$

If a particle A is initially free at $t = 0$, the probability to find it in the free state after Δt is given by

$$F_{A}(\Delta t) = F_{eq}\left(1 + K_{eq}^{*}e^{-(k_{on}^{*}+k_{off})\Delta t}\right). \qquad \text{[S3]}$$

Here, $K_{eq}^{*} = k_{on}^{*}/k_{off}$ is the pseudoequilibrium binding constant. In contrast, if a particle B is initially bound at $t = 0$, the probability to find it in the free state after Δt reads

$$F_{B}(\Delta t) = F_{eq}\left(1 - e^{-(k_{on}^{*}+k_{off})\Delta t}\right). \qquad \text{[S4]}$$

The quantities $F_{A}(\Delta t)$ and $F_{B}(\Delta t)$ can also be regarded as the fraction of time that the particles have spent in the free state during Δt. Because complexes are assumed to be immobile, particles can only diffuse during their time in the free state. Thus, the apparent diffusion coefficient of the particles A and B is reduced because they are trapped part of the time. This apparent diffusion coefficient corresponds to the weighted average of the diffusion coefficients in the free state and the bound state, which, for a diffusion coefficient $D_{bound} \sim 0$ in the bound state, yields

$$D_{A}(\Delta t) = DF_{A}(\Delta t) = DF_{eq}\left(1 + K_{eq}^{*}e^{-(k_{on}^{*}+k_{off})\Delta t}\right)$$
$$D_{B}(\Delta t) = DF_{B}(\Delta t) = DF_{eq}\left(1 - e^{-(k_{on}^{*}+k_{off})\Delta t}\right). \qquad \text{[S5]}$$

For large times $\Delta t >> (k_{on}^{*} + k_{off})^{-1}$, both apparent diffusion coefficients converge to the effective diffusion coefficient $D_{eff} =$

$DF_{eq} = D/(1 + K_{eq}^{*})$ (1). For small values of $\Delta t << (k_{on}^{*} + k_{off})^{-1}$, $D_{A} \rightarrow D$ and $D_{B} \rightarrow 0$, which reflect the initial conditions that particle A is free at $t = 0$ and particle B is bound at $t = 0$ (Fig. S1B). The average diffusion coefficient for the ensemble is the weighted average of the apparent diffusion coefficients D_{A} and D_{B} of the two pools (i.e., pool A with particles being initially free and pool B with particles being initially bound). Because the probability to find a free particle at $t = 0$ is F_{eq} and the probability to find a bound one is C_{eq}, the average diffusion coefficient is given by

$$D_{avg} = F_{eq}D_{A}(\Delta t) + C_{eq}D_{B}(\Delta t)$$
$$= F_{eq}DF_{eq}\left(1 + K_{eq}^{*}e^{-(k_{on}^{*}+k_{off})\Delta t}\right) + C_{eq}DF_{eq}\left(1 - e^{-(k_{on}^{*}+k_{off})\Delta t}\right)$$
$$= DF_{eq}(F_{eq} + C_{eq}) = \frac{D}{1 + K_{eq}^{*}} = D_{eff}. \qquad \text{[S6]}$$

As expected, the diffusion coefficient for the ensemble is not time-dependent and equals the effective diffusion coefficient. Thus, although the ensemble diffusion coefficient is D_{eff} on all time scales, the ensemble decomposes into a free pool and a bound pool on small time scales $\Delta t << (k_{on}^{*} + k_{off})^{-1}$, whereas the mobilities of the pools become similar for $\Delta t >> (k_{on}^{*} + k_{off})^{-1}$ (Fig. S1 B and C). In the first case, the size and the diffusion coefficient D of the free pool can be measured and the ratio of the rate constants $K_{eq}^{*} = k_{on}^{*}/k_{off}$ can be obtained from $F_{eq} = 1/(1 + K_{eq}^{*})$. This requires the accurate quantification of the free and immobile fractions. In the second case, only the effective diffusion coefficient D_{eff} can be determined. If the free diffusion coefficient is known, $K_{eq}^{*} = k_{on}^{*}/k_{off}$ can be calculated from the effective diffusion coefficient. In both scenarios, individual rate constants cannot be resolved because these can only be obtained from measurements on the intermediate time scale. In this regime, particles exchange between free pool and bound pool, and provide information about the binding reaction (Fig. S1C). Because conventional fluorescence recovery after photobleaching (FRAP) and fluorescence correlation spectroscopy (FCS) implementations are limited in their accessible time scales, only a distinct subset of kinetic rate constants can be determined that matches the relation $\Delta t \approx (k_{on}^{*} + k_{off})^{-1}$ (1, 2). In contrast, methods like raster image correlation spectroscopy, pair correlation analysis, or pixel-wise photobleaching evolution analysis (3PEA) include measurements on multiple scales, and thus cover a larger range of rates measurable for reaction-diffusion processes.

Derivation of the Theoretical 3PEA Framework for Free Diffusion.
Bleaching a Point. In the following, an expression is derived that yields the probability for a particle to be bleached at pixel position $\vec{x}_0$ and to be subsequently detected via a decrease of the fluorescence signal when the focus is located at pixel position $\vec{x}_1$. The point spread functions (PSFs) are approximated by 3D-Gaussian geometry. This is sufficiently accurate for all experimentally relevant scenarios of this study because the 3PEA method relies on pixel distances rather than on the exact shape of the PSF. The equations derived here apply to normal diffusion. To account for other models or binding interactions, the diffusion propagator in the equations below is substituted with the corresponding expression. Thus, the theoretical description presented here can be used for any type of translocation process.

In the first step, we consider the probability P_{bleach} for a particle located at $\vec{x}$ to be bleached while the focus is located at $\vec{x}_0$. Assuming that bleaching is a first-order process with a bleach rate proportional to the illumination intensity, the amount

of fluorescent particles decreases with $\exp(-\gamma PSF^{1/2}\tau_{\text{bleach}}) \approx 1 - \gamma PSF^{1/2}\tau_{\text{bleach}}$. Here, the PSF is defined according to Eq. 3 as the product of the illumination and detection PSF. Accordingly, the PSF for the bleaching process is given by

boids (Fig. S1). The intensity differences within a single cuboid are neglected, and the integral in Eq. S10 is divided into two parts: the average cuboid bleach probability $\langle P_{\text{bleach},i}\rangle$ and the translocation probability $P^{\text{r2c}}_{x_i \to x_1}$:

$$
\begin{aligned}
N^{\text{r2c}}_{x_0 \to x_1}(\vec{x}_0, \vec{x}_1, \Delta t) &= \sum_i c\langle P_{\text{bleach},i}\rangle(\vec{x}_0) \int\limits_{-\infty}^{\infty} dx' \int\limits_{-\infty}^{\infty} dy' \int\limits_{-\infty}^{\infty} dz'\ \Psi_{\text{det}}(\vec{x}', \vec{x}_1) \int\limits_{x_i-r_x}^{x_i+r_x} dx \int\limits_{y_i-r_y}^{y_i+r_y} dy \int\limits_{z_i-r_z}^{z_i+r_z} dz\ P_{\text{diff}}(\vec{x}, \vec{x}', \Delta t) \\
&= \sum_i \frac{cV_{\text{eff}}}{8}\langle P_{\text{bleach},i}\rangle(\vec{x}_0) \left[\text{erf}\left(\frac{x_i - x_1 + r_x}{\sqrt{w_0^2/2 + d^2}}\right) - \text{erf}\left(\frac{x_i - x_1 - r_x}{\sqrt{w_0^2/2 + d^2}}\right) \right] \\
&\quad \times \left[\text{erf}\left(\frac{y_i - y_1 + r_y}{\sqrt{w_0^2/2 + d^2}}\right) - \text{erf}\left(\frac{y_i - y_1 - r_y}{\sqrt{w_0^2/2 + d^2}}\right) \right] \left[\text{erf}\left(\frac{z_i - z_1 + r_z}{\sqrt{z_0^2/2 + d^2}}\right) - \text{erf}\left(\frac{z_i - z_1 - r_z}{\sqrt{z_0^2/2 + d^2}}\right) \right],
\end{aligned}
\tag{S11}
$$

$PSF^{1/2}$. Because τ_{bleach} is the pixel time that is typically of the order of some microseconds, the latter approximation is appropriate, and the bleach probability can be expressed as

$$
\begin{aligned}
P_{\text{bleach}}(\vec{x}, \vec{x}_0) &= \beta PSF^{1/2}(\vec{x}, \vec{x}_0) \\
&= \beta \exp\left(-\frac{(x-x_0)^2 + (y-y_0)^2}{w_b^2} - \frac{(z-z_0)^2}{z_b^2}\right). \quad \text{[S7]}
\end{aligned}
$$

In Eq. S7, $\beta = \gamma\tau_{\text{bleach}} \leq 1$ is the bleach depth, and w_b and z_b denote the effective beam waist of the bleach PSF in lateral and axial directions, respectively. Because the high laser intensities during the bleach typically lead to an enlarged PSF, the specific set of structure parameters (w_b, z_b) is used to describe the bleach PSF.

In the second step, the probability P_{diff} for a particle located at $\vec{x}$ to diffuse to $\vec{x}'$ during time Δt is calculated. This probability is

$$
P_{\text{diff}}(\vec{x}, \vec{x}', \Delta t) = \frac{1}{(\pi d^2(\Delta t))^{3/2}} \exp\left(-\frac{(x-x')^2 + (y-y')^2 + (z-z')^2}{d^2(\Delta t)}\right). \quad \text{[S8]}
$$

Here, D is the diffusion coefficient and $d^2(\Delta t) = 4D\Delta t$ is the particle's mean squared displacement (MSD) for normal diffusion. Finally, the fluorescence intensity Ψ_{det} of a particle located at $\vec{x}'$ in the focus at $\vec{x}_1$ is calculated with Eq. S9:

$$
\begin{aligned}
\Psi_{\text{det}}(\vec{x}', \vec{x}_1) &= PSF(\vec{x}', \vec{x}_1) \\
&= \exp\left(-2\frac{(x'-x_1)^2 + (y'-y_1)^2}{w_0^2} - 2\frac{(z'-z_1)^2}{z_0^2}\right). \quad \text{[S9]}
\end{aligned}
$$

Based on Eqs. S7, S8, and S9, the fluorescence intensity reduction in $\vec{x}_1$ caused by particles bleached in $\vec{x}_0$ is proportional to

$$
\begin{aligned}
N^{\text{r2c}}_{x_0 \to x_1}(\vec{x}_0, \vec{x}_1, \Delta t) &= c \int\limits_{-\infty}^{\infty} dx' \int\limits_{-\infty}^{\infty} dy' \int\limits_{-\infty}^{\infty} dz'\ \Psi_{\text{det}}(\vec{x}', \vec{x}_1) \\
&\quad \times \int\limits_{-\infty}^{\infty} dx \int\limits_{-\infty}^{\infty} dy \int\limits_{-\infty}^{\infty} dz\ P_{\text{bleach}}(\vec{x}, \vec{x}_0)P_{\text{diff}}(\vec{x}, \vec{x}', \Delta t). \quad \text{[S10]}
\end{aligned}
$$

Because overlapping bleach PSFs have to be considered for 2D bleach regions, the bleach PSF is split up into a sum of cu-

with the average cuboid bleach probability $\langle P_{\text{bleach},i}\rangle(\vec{x}_0) = \frac{1}{V_{b,i}} \int_{x_i-r_x}^{x_i+r_x} dx \int_{y_i-r_y}^{y_i+r_y} dy \int_{z_i-r_z}^{z_i+r_z} dz\ P_{\text{bleach}}(\vec{x}, \vec{x}_0)$.

Each part of the sum in Eq. S11 gives the reduced intensity due to the presence of particles bleached in a single cuboid centered at $\vec{x}_i$ with edge lengths $2r_x$, $2r_y$, and $2r_z$ and volume $V_{b,i}$. For high laser intensities, which are typically used for FRAP experiments, the axial beam waist becomes very large. For this case (i.e., in the limit $z_b \to \infty$, $r_z \to \infty$), the axial dependence can be neglected and Eq. S11 is written as

$$
N^{\text{r2c*}}_{x_0 \to x_1}(\vec{x}_0, \vec{x}_1, \Delta t) = cV_{\text{eff}} \sum_i \langle P_{\text{bleach},i}\rangle P^{\text{r2c*}}_{x_i \to x_1}(\vec{x}_i, \vec{x}_1, \Delta t), \quad \text{[S12]}
$$

with

$$
\begin{aligned}
P^{\text{r2c*}}_{x_i \to x_1} &= \frac{1}{4}\left[\text{erf}\left(\frac{x_i - x_1 + r_x}{\sqrt{w_0^2/2 + d^2}}\right) - \text{erf}\left(\frac{x_i - x_1 - r_x}{\sqrt{w_0^2/2 + d^2}}\right) \right] \\
&\quad \times \left[\text{erf}\left(\frac{y_i - y_1 + r_y}{\sqrt{w_0^2/2 + d^2}}\right) - \text{erf}\left(\frac{y_i - y_1 - r_y}{\sqrt{w_0^2/2 + d^2}}\right) \right].
\end{aligned}
$$

Bleaching a Line. For typical scan speeds, the line time τ_l is on the order of 1 ms. This corresponds to the dwell time of a freely mobile protein in one diffraction-limited spot. Therefore, diffusion during the bleach process of a single bleach line (or a line segment) can be simplified to reduce the computational cost of the calculations significantly. Based on the bleach probability in a single spot (Eqs. S7–S12), the bleach distribution after sequentially bleaching several spots along a line is derived. The intensity in $\vec{x}$ after n bleach events at positions $\vec{x}_i$ is given by

$$
\begin{aligned}
I(\vec{x}, n) &= 1 - P_{\text{bleach}}(\vec{x}, n) = \prod_{i=0}^{n}\left(1 - \beta PSF^{1/2}(\vec{x}, \vec{x}_i)\right) \\
&= \exp\left(\ln\left(\prod_{i=0}^{n}\left(1 - \beta PSF^{1/2}(\vec{x}, \vec{x}_i)\right)\right)\right) \\
&= \exp\left(\sum_{i=0}^{n}\ln\left(1 - \beta \exp\left(-\frac{(x-x_i)^2 + (y-y_0)^2}{w_b^2} - \frac{(z-z_0)^2}{z_b^2}\right)\right)\right).
\end{aligned}
\tag{S13}
$$

Thus, if a line between $-x_b$ and x_b is bleached, the intensity distribution can be expressed as

$$I(\vec{x}, \vec{x}_0, \vec{x}_b) = 1 - P_{\text{bleach}}(\vec{x}, \vec{x}_b) = \exp\left(\int\limits_{-x_b}^{x_b} dx_i \mu \ln\left(1 - \beta \exp\left(-\frac{(x-x_i)^2 + (y-y_0)^2}{w_b^2} - \frac{(z-z_0)^2}{z_b^2} \right) \right) \right), \qquad \textbf{[S14]}$$

with an effective line bleach probability μ. To solve the integral given in Eq. **S14**, the logarithm is represented by a series expansion, yielding

$$P_{\text{bleach}}^{\text{line}}(\vec{x}, \vec{x}_0, \vec{x}_b) = 1 - \exp\left(\int\limits_{-x_b}^{x_b} dx_i \mu \sum_{n=1}^{\infty} \frac{(-1)^{n+1}}{n} \left(-\beta \exp\left(-\frac{(x-x_i)^2 + (y-y_0)^2}{w_b^2} - \frac{(z-z_0)^2}{z_b^2} \right) \right)^n \right)$$

$$= 1 - \exp\left(-\sum_{n=1}^{\infty} \frac{\mu}{n} \left(\beta \exp\left(-\frac{(y-y_0)^2}{w_b^2} - \frac{(z-z_0)^2}{z_b^2} \right) \right)^n \int\limits_{-x_b}^{x_b} dx_i \exp\left(-n\frac{(x-x_i)^2}{w_b^2} \right) \right)$$

$$= 1 - \exp\left(-\frac{\sqrt{\pi}}{2} \sum_{n=1}^{\infty} \frac{\mu w_n}{n} \left(\beta \exp\left(-\frac{(y-y_0)^2}{w_b^2} - \frac{(z-z_0)^2}{z_b^2} \right) \right)^n \left(\text{erf}\left(\frac{x+x_b}{w_n} \right) - \text{erf}\left(\frac{x-x_b}{w_n} \right) \right) \right), \qquad \textbf{[S15]}$$

with $w_n = \frac{w_b}{\sqrt{n}}$. The series in the exponential function decreases monotonically and the expression in the last line of Eq. **S15** converges. The series can be truncated as needed to compute the results numerically with the desired accuracy. For the calculations conducted here, the series was truncated at $n = 500$ and the bleach parameters $\beta = 0.2$ and $\mu = 2$ per pixel were used. In analogy to Eq. **S12**, the number of particles that translocate from a pixel $\vec{x}_0$ within the bleached line into pixel $\vec{x}_1$ can be calculated by replacing $P_{\text{bleach}}(\vec{x}, \vec{x}_0)$ with the line bleach probability $P_{\text{bleach}}^{\text{line}}(\vec{x}, \vec{x}_0)$ given in Eq. **S15**. The time stamp for each bleach event was assigned based on its x-position along the line. Thus, the sequential bleach events were correctly separated in time; however, their PSF was not assumed to be a Gaussian distribution but rather a slice of the line bleach PSF in Eq. **S15**. For pixels adjacent to the designated bleach spot that are bleached due to the spatial extension of the bleach PSF, the time stamp corresponding to the first/last point of the bleach region in the current scan line was assigned. This approach introduces errors in the bleach times that are on the order of the time the microscope's beam needs to translocate the distance that equals the lateral width of the bleach PSF, which is below 1 μm. For a scan speed of 1,400 Hz, a pixel time of roughly 0.4 μs, and a voxel size of 7.5 nm, this error is smaller than 50 μs.

Bleaching a 2D Region. In this section, the intensity distribution after bleaching a 2D region is derived. First, the fraction of particles bleached in a pixel of such a bleach region is calculated. This probability is not equal in all bleach pixels/lines. A particle can already be bleached when the focus is located at a precedent pixel/line due to the spatial extension of the bleach PSF and diffusive transport during the bleach process. The fraction of particles bleached in pixel $\vec{x}$ in the bleach region can be expressed with the recursive relation

$$N_{\text{bleach}}(\vec{x}, t) = P_{\text{bleach}}(\vec{x}, \vec{x}_0)$$
$$\times \left(\langle N \rangle - \sum_{t_i < t} \sum_{\vec{x}' \in \text{PSF}_i} N_{\text{bleach}}(\vec{x}', t_i) \, P_{x' \to x}^{\text{r2r}}(\vec{x}', \vec{x}, t - t_i) \right). \quad \textbf{[S16]}$$

The probability $P_{x' \to x}^{\text{r2r}}(\vec{x}', \vec{x}, \Delta t)$ is the probability for a particle to be present in pixel $\vec{x}'$ and to translocate to pixel $\vec{x}$ during the time interval Δt. For cuboid voxels, this probability is given by

$$P_{x' \to x}^{\text{r2r}}(\vec{x}', \vec{x}, \Delta t) = \int\limits_{x'-r_x}^{x'+r_x} d\bar{x} \int\limits_{y'-r_y}^{y'+r_y} d\bar{y} \int\limits_{z'-r_z}^{z'+r_z} d\bar{z} \int\limits_{x-r_x}^{x+r_x} d\hat{x} \int\limits_{y-r_y}^{y+r_y} d\hat{y}$$

$$\times \int\limits_{z-r_z}^{z+r_z} d\hat{z} \; P_{\text{diff}}(\vec{\bar{x}}, \vec{\hat{x}}, \Delta t) = \frac{1}{8} XYZ, \qquad \textbf{[S17]}$$

with the following abbreviations:

$$X = (\Delta x + 2r_x)\text{erf}\left(\frac{\Delta x + 2r_x}{d} \right) + (\Delta x - 2r_x)\text{erf}\left(\frac{\Delta x - 2r_x}{d} \right)$$
$$- 2\Delta x \, \text{erf}\left(\frac{\Delta x}{d} \right) + \sqrt{\frac{d^2}{\pi}} \left(e^{-\frac{(\Delta x + 2r_x)^2}{d^2}} + e^{-\frac{(\Delta x - 2r_x)^2}{d^2}} - 2e^{-\frac{\Delta x^2}{d^2}} \right)$$

$$Y = (\Delta y + 2r_y)\text{erf}\left(\frac{\Delta y + 2r_y}{d} \right) + (\Delta y - 2r_y)\text{erf}\left(\frac{\Delta y - 2r_y}{d} \right)$$
$$- 2\Delta y \, \text{erf}\left(\frac{\Delta y}{d} \right) + \sqrt{\frac{d^2}{\pi}} \left(e^{-\frac{(\Delta y + 2r_y)^2}{d^2}} + e^{-\frac{(\Delta y - 2r_y)^2}{d^2}} - 2e^{-\frac{\Delta y^2}{d^2}} \right)$$

$$Z = (\Delta z + 2r_z)\text{erf}\left(\frac{\Delta z + 2r_z}{d} \right) + (\Delta z - 2r_z)\text{erf}\left(\frac{\Delta z - 2r_z}{d} \right)$$
$$- 2\Delta z \, \text{erf}\left(\frac{\Delta z}{d} \right) + \sqrt{\frac{d^2}{\pi}} \left(e^{-\frac{(\Delta z + 2r_z)^2}{d^2}} + e^{-\frac{(\Delta z - 2r_z)^2}{d^2}} - 2e^{-\frac{\Delta z^2}{d^2}} \right)$$

Here, d^2 is the particles' MSD and $\Delta x = \hat{x} - \tilde{x}$, $\Delta y = \hat{y} - \tilde{y}$, and $\Delta z = \hat{z} - \tilde{z}$. Based on Eqs. **S16** and **S17**, the intensity distribution after an arbitrary number of bleach events can be expressed according to

$$I(\vec{x}, t) = \varepsilon \left(\langle N \rangle - \sum_{t_i} \sum_{\vec{x}' \in \text{PSF}_i} N_{\text{bleach}}\left(\vec{x}', t_i \right) P_{x' \to x}^{\text{r2c}}\left(\vec{x}', \vec{x}, t - t_i \right) \right). \quad \textbf{[S18]}$$

3PEA for Reaction-Diffusion Processes. To apply 3PEA in the presence of reaction-diffusion processes, the propagator in Eq. S8 is replaced with an expression that accounts for binding interactions. This reaction-diffusion propagator is derived in the following. The starting point is the dissociation of particles from a binding site, which is described by the differential equation

$$\frac{dN(t)}{dt} = -k_{\mathrm{off}} N(t), \qquad \text{[S19]}$$

with the solution $N(t) = N_0\, e^{-k_{\mathrm{off}} t}$. Thus, the probability for a bound particle to remain at the binding site for the time t_{res} is $P_{\mathrm{b}}(t_{\mathrm{res}}) = k_{\mathrm{off}}\, e^{-k_{\mathrm{off}} t_{\mathrm{res}}}$, where the prefactor is required for normalization. The probability distribution for an arbitrary particle's residence time t_{res} in the presence of binding reactions with pseudoassociation rate k_{on}^* and dissociation rate k_{off} is

$$P_{\mathrm{bound}}(t_{\mathrm{res}}) = F_{\mathrm{eq}}\delta(t_{\mathrm{res}}) + C_{\mathrm{eq}} k_{\mathrm{off}} e^{-k_{\mathrm{off}} t_{\mathrm{res}}}. \qquad \text{[S20]}$$

Here, $F_{\mathrm{eq}} = \frac{k_{\mathrm{off}}}{k_{\mathrm{on}}^* + k_{\mathrm{off}}}$ and $C_{\mathrm{eq}} = \frac{k_{\mathrm{on}}^*}{k_{\mathrm{on}}^* + k_{\mathrm{off}}}$ are the free and bound fractions in steady state, respectively (see above). The first term is the probability to find a free particle, and the second term is the probability to find a particle bound for t_{res}. With this result, the propagator in Eq. S8 can be redefined as

$$P_{\mathrm{reac+diff}}(\vec{x}_0, \vec{x}_1, \Delta t) = F_{\mathrm{eq}} P_{\mathrm{diff}}(\vec{x}_0, \vec{x}_1, \Delta t \cdot F_{\mathrm{A}}(\Delta t))$$
$$+ C_{\mathrm{eq}} \int_0^{\Delta t} dt_{\mathrm{res}}\, k_{\mathrm{off}} e^{-k_{\mathrm{off}} t_{\mathrm{res}}} P_{\mathrm{diff}}(\vec{x}_0, \vec{x}_1, (\Delta t - t_{\mathrm{res}})$$
$$\cdot F_{\mathrm{A}}(\Delta t - t_{\mathrm{res}})) + C_{\mathrm{eq}} e^{-k_{\mathrm{off}} \Delta t} \delta(\vec{x}_0 - \vec{x}_1). \qquad \text{[S21]}$$

Here, $F_{\mathrm{A}}(t)$ is the fraction of time a particle spends in the free state if it was free at $t = 0$ (derived above in Eq. S3). The first line of Eq. S21 represents particles that are initially free and subsequently diffuse for $\Delta t \cdot F_{\mathrm{A}}(\Delta t)$. The second line represents particles that are initially bound, dissociate after $t_{\mathrm{res}} < \Delta t$, and diffuse for the rest of the time they spend in the free state [i.e., $(\Delta t - t_{\mathrm{res}}) \cdot F_{\mathrm{A}}(\Delta t - t_{\mathrm{res}})$]. The third line represents particles that are initially bound and remain bound for $t_{\mathrm{res}} > \Delta t$.

In general, the integral in the second line of Eq. S21 has to be solved numerically. For special cases, an analytical reaction-diffusion propagator can be found. One case is binding that is much slower than the time scale of the measurement (i.e., $k_{\mathrm{off}}^{-1} \gg \Delta t$). Here, the probability to dissociate from a binding site within Δt can be neglected [i.e., $P_{\mathrm{b}}(t_{\mathrm{res}} < \Delta t) \to 0$] and the integrand in Eq. S21 vanishes. The propagator converges to the sum of a diffusing pool and an immobile pool, with both having analytical propagators. For binding that occurs much faster than the time scale of the measurement (i.e., $k_{\mathrm{off}}^{-1} \ll \Delta t$), the integrand in Eq. S21 vanishes as well and one effectively diffusing pool with diffusion coefficient D_{eff} remains.

Convergence of 3PEA in the Limit of Infinitely Fast Scanning. In the limit of infinitely fast scanning and negligible beam waist, the above theoretical description yields the state-of-the-art FRAP model for a uniform disk derived previously (1, 3). For free diffusion, the probability to bleach a particle in $\vec{x}_0$ and to detect it in $\vec{x}_1$ (as fluorescence intensity decrease) is given by

$$P_{\mathrm{x}_0 \to \mathrm{x}_1}^{\mathrm{lim}}(\vec{x}_0, \vec{x}_1, \Delta t) = \frac{\beta}{4\pi D \Delta t} e^{\frac{(x_1 - x_0)^2 + (y_1 - y_0)^2}{4 D \Delta t}}. \qquad \text{[S22]}$$

In case of infinitely fast scanning, the time Δt corresponds to the time τ_{f} to acquire one image frame. The number of bleached particles is equal in every pixel (i.e., Eq. 5 is not required). To obtain the intensity profile after having bleached a circle with radius R located around the center of the image (0, 0), the sum in Eq. 6 is replaced by an integral:

$$I(\vec{x}, m) = \varepsilon \langle N \rangle \left(1 - \int_{\vec{x}' \in \mathrm{ROI}} d\vec{x}'\, P_{x' \to x}^{\mathrm{lim}}(\vec{x}', \vec{x}, m\tau_{\mathrm{f}}) \right)$$
$$= \varepsilon \langle N \rangle \left(1 - \frac{\beta}{4\pi D m \tau_{\mathrm{f}}} \int_0^R r r' dr' \int_0^{2\pi} d\phi'\, e^{\frac{r^2 + r'^2 - 2rr'\cos\phi'}{4 D m \tau_{\mathrm{f}}}} \right)$$
$$= \varepsilon \langle N \rangle \left(1 - \frac{\beta}{2 D m \tau_{\mathrm{f}}} \int_0^R r r' e^{-\frac{r^2 + r'^2}{4 D m \tau_{\mathrm{f}}}} dr'\, I_0\!\left(\frac{rr'}{2 D m \tau_{\mathrm{f}}} \right) \right). \qquad \text{[S23]}$$

Here, $I_0(x)$ denotes the modified Bessel function of the first kind and m is the number of the postbleach frame. In the last step, the integral representation of $I_0(x)$ was used. The integral in the last line of Eq. S23 corresponds to the one used by Soumpasis (equation 9 of ref. 3) to derive the well-known FRAP model for free diffusion; for $\beta = 1$, this is given by

$$I_{\mathrm{ROI}}(m) = \int_{\vec{x} \in \mathrm{ROI}} d\vec{x}\, I(\vec{x}, m)$$
$$= \varepsilon \langle N \rangle\, e^{-\frac{R^2}{2 D m \tau_{\mathrm{f}}}} \left[I_0\!\left(\frac{R^2}{2 D m \tau_{\mathrm{f}}} \right) + I_1\!\left(\frac{R^2}{2 D m \tau_{\mathrm{f}}} \right) \right]. \qquad \text{[S24]}$$

In analogy to the calculations above, the 3PEA limit for infinitely fast scanning and negligible beam waist in the presence of a reaction-diffusion process is derived as described below. Similar to Eq. S22, the probability to bleach a particle in $\vec{x}_0$ and to find it in $\vec{x}_1$ for the case of diffusion and binding (based on Eqs. S20 and S21) amounts to

$$P_{\mathrm{b}, \mathrm{x}_0 \to \mathrm{x}_1}^{\mathrm{lim}}(\vec{x}_0, \vec{x}_1, \Delta t) = \left(P_{\mathrm{bound}} \otimes P_{\mathrm{x}_0 \to \mathrm{x}_1}^{\mathrm{lim}} \right)(\vec{x}_0, \vec{x}_1, \Delta t)$$
$$+ C_{\mathrm{eq}} e^{-k_{\mathrm{off}} \Delta t} \delta(\vec{x}_0, \vec{x}_1). \qquad \text{[S25]}$$

Here, $\otimes$ is the convolution operator. In the limit of vanishing beam waist, the Dirac delta distribution is obtained; the bleach depth was set to $\beta = 1$. The relation between the integrated intensity in the bleach region of interest and the transition probability in Eq. S25 is given by

$$I_{\mathrm{ROI}}(m) = \int_{\vec{x} \in \mathrm{ROI}} I(\vec{x}, m)$$
$$= \varepsilon \langle N \rangle \left(1 - \int_{\vec{x} \in \mathrm{ROI}} d\vec{x} \int_{\vec{x} \in \mathrm{ROI}} d\vec{x}'\, P_{\mathrm{b}, x' \to x}^{\mathrm{lim}}(\vec{x}', \vec{x}, m\tau_{\mathrm{f}}) \right)$$
$$= \varepsilon \langle N \rangle \left(1 - \int_{\vec{x} \in \mathrm{ROI}} d\vec{x} \int_{\vec{x}' \in \mathrm{ROI}} d\vec{x}'\, (P_{\mathrm{bound}} \otimes P_{\mathrm{x}' \to \mathrm{x}}^{\mathrm{lim}}) \right.$$
$$\left. (\vec{x}', \vec{x}, m\tau_{\mathrm{f}}) - C_{\mathrm{eq}} e^{-k_{\mathrm{off}} m \tau_{\mathrm{f}}} \right). \qquad \text{[S26]}$$

Because the convolution in Eq. S26 cannot be calculated analytically, an expression for the Laplace-transformed intensity is derived. Starting from the Laplace transform for the pure dif-

fusion case (1), together with the results from the previous section, the following relation is obtained:

$$
\bar{I}_{\text{ROI}}(p) = \varepsilon \langle N \rangle L \left\{ 1 - \int\limits_{\vec{x} \in \text{ROI}} d\vec{x} \int\limits_{\vec{x}' \in \text{ROI}} d\vec{x}' \, P_{x' \to x}^{\lim}\left(\vec{x}', \vec{x}, t\right) \right\}
$$
$$
= \varepsilon \langle N \rangle \left(\frac{1}{p} - \frac{1}{p} \left(1 - 2K_1\left(R\sqrt{\frac{p}{D}}\right) I_1\left(R\sqrt{\frac{p}{D}}\right) \right) \right).
$$

[S27]

Here, $L\{f(t)\}$ denotes the Laplace transform. Thus, for the case of binding and diffusion, Eq. S27 reads

$$
\bar{I}_{\text{ROI}}(p) = \varepsilon \langle N \rangle \left(\frac{1}{p} - L \left\{ \int\limits_{\vec{x} \in \text{ROI}} d\vec{x} \int\limits_{\vec{x}' \in \text{ROI}} d\vec{x}' \right. \right.
$$
$$
\left. \left(P_{\text{bound}} \otimes P_{x' \to x}^{\lim}\right)\left(\vec{x}', \vec{x}, t\right) + C_{\text{eq}} e^{-k_{\text{off}} t} \right\} \right)
$$
$$
= \varepsilon \langle N \rangle \left(\frac{1}{p} - L\{P_{\text{bound}}(t)\} \int\limits_{\vec{x} \in \text{ROI}} d\vec{x} \int\limits_{\vec{x}' \in \text{ROI}} d\vec{x}' \right.
$$
$$
\left. L\left\{ P_{x' \to x}^{\lim}\left(\vec{x}', \vec{x}, t'\right) \right\} - C_{\text{eq}} L\{e^{-k_{\text{off}} t}\} \right)
$$
$$
= \varepsilon \langle N \rangle \left(\frac{1}{p} - \frac{1}{p} L\{P_{\text{bound}}(t)\} \left(1 - 2K_1\left(\sqrt{p'}\right) I_1\left(\sqrt{p'}\right) \right) - \frac{C_{\text{eq}}}{p + k_{\text{off}}} \right).
$$

[S28]

In the first step, the convolution theorem for Laplace transforms was used. Furthermore, the dimensionless variable $t' = t \frac{D_A(t)}{R^2}$ with its Laplace variable $p' = p\frac{R^2}{\bar{D}(p)} = \frac{R^2}{L\{D_A(t)\}}$ was introduced. The solution for $L\{P_{\text{bound}}(t)\}$ with $P_{\text{bound}}(t)$ as defined in Eq. S20 is

$$
L\{P_{\text{bound}}(t)\} = F_{\text{eq}} L\{\delta(t)\} + C_{\text{eq}} k_{\text{off}} L\left\{ e^{-k_{\text{off}} t_{\text{res}}} \right\}
$$
$$
= \left(F_{\text{eq}} + C_{\text{eq}} \frac{k_{\text{off}}}{p + k_{\text{off}}} \right) = F_{\text{eq}} \left(1 + \frac{k_{\text{on}}^*}{p + k_{\text{off}}} \right).
$$

[S29]

Based on Eqs. S28 and S29, the expression for the Laplace-transformed intensity in the bleach spot can be written as

$$
\bar{I}_{\text{ROI}}(p) = \varepsilon \langle N \rangle \left(\frac{1}{p} - \frac{1}{p} F_{\text{eq}} \left(1 + \frac{k_{\text{on}}^*}{p + k_{\text{off}}} \right) \left(1 - 2K_1\left(\sqrt{p'}\right) I_1\left(\sqrt{p'}\right) \right) \right.
$$
$$
\left. - \frac{C_{\text{eq}}}{p + k_{\text{off}}} \right),
$$

[S30]

with $p' = p\frac{R^2}{\bar{D}(p)} = \frac{pR^2}{D}\left(1 + \frac{k_{\text{on}}^*}{p + k_{\text{off}}} \right)$.

This is the result obtained previously for reaction-diffusion processes by Sprague et al. (1).

Calculating Effective Translocation Probability Distributions. Based on the microscope's scan parameters, the characteristic spatial and temporal distance to a set of bleach events can be calculated for every pixel of the image. The characteristic temporal distance was determined according to

$$
\overline{\Delta t} = \frac{\sum\limits_{\vec{x} \in \text{ROI}} \sum\limits_{\vec{x}' \in \text{PSF}} \Delta t\left(\vec{x}, \vec{x}'\right) \cdot |\vec{x} - \vec{x}'|^{-1}}{\sum\limits_{\vec{x} \in \text{ROI}} \sum\limits_{\vec{x}' \in \text{PSF}} |\vec{x} - \vec{x}'|^{-1}}.
$$

[S31]

Here, $\Delta t(\vec{x}, \vec{x}')$ represents the temporal distance between pixels $\vec{x}$ and $\vec{x}'$ (according to Eq. 1). The $|\vec{x}-\vec{x}'|^{-1}$ term is a weight factor accounting for the fact that particles diffusing larger distances are underrepresented in a given pixel, because in a 2D process, every pixel $\vec{x}'$ can be regarded as a radial line segment of a circle around the originating pixel $\vec{x}$. For simplicity, it was neglected that bleaching also occurs at pixels outside the nominal bleach region due to the spatial extension of the PSF. The characteristic spatial distance was calculated in an analogous manner:

$$
\overline{\Delta x} = \frac{\sum\limits_{\vec{x} \in \text{ROI}} \sum\limits_{\vec{x}' \in \text{PSF}} \Delta x\left(\vec{x}, \vec{x}'\right) \cdot |\vec{x} - \vec{x}'|^{-1}}{\sum\limits_{\vec{x} \in \text{ROI}} \sum\limits_{\vec{x}' \in \text{PSF}} |\vec{x} - \vec{x}'|^{-1}}.
$$

[S32]

Similar to Eq. S31, $\Delta x(\vec{x}, \vec{x}') = |\vec{x} - \vec{x}'|$ represents the spatial distance between pixels $\vec{x}$ and $\vec{x}'$. Based on the assignment of Δx and Δt, translocation probabilities can be estimated from the pixel intensities as explained in the main text.

3PEA Implementation. The workflow for the 3PEA data analysis of protein mobility in the presence of interactions with immobile obstacles, such as chromatin, is illustrated in Fig. S7. The experimental bleach profile is fitted with the diffusion library to determine the apparent diffusion coefficient D. The value of D retrieved from the diffusion fit is compared with the free diffusion coefficient D_{free} that can be derived by different approaches: (*i*) The protein mobility in the cytosol can be measured, which yields D in the absence of chromatin interactions; (*ii*) a similar-sized inert protein can be measured, such as, for example, the green autofluorescent protein (GFP) pentamer used here; and (*iii*) the diffusion coefficient can be calculated based on its molecular weight and/or structure (4). A value of the apparent diffusion coefficient D similar to D_{free} indicates that binding interactions can be neglected. If D is significantly smaller than D_{free}, it is likely that binding reactions decrease protein mobility. Other reasons for a reduced diffusion coefficient include caging effects or the formation of a multimeric protein complex that displays an increased molecular weight M over that of the monomeric protein, with D being proportional to $M^{-1/3}$ for a spherical protein. However, these contributions typically lead to only moderate changes. Protein complexes with M as high as 1–2 MDa appear to be unrestricted in terms of the accessible nuclear space (5), and up to a GFP pentamer, protein mobilities were found to be very similar in the cytoplasm and in the nucleoplasm (6). In the case of protein binding, the interaction with chromatin is described by a pseudoequilibrium constant $K^*_{\text{eq}} = k^*_{\text{on}}/k_{\text{off}}$, with k^*_{on} also including the concentration of binding sites according to the formalism outlined above. To separate the diffusion of the protein from the binding contribution, the bleach profile is fitted to a reaction-diffusion model. If both the diffusion and the reaction-diffusion fits are of similar quality, a transient binding interaction is present that is included in the value of the effective diffusion coefficient. Otherwise, the fit to the full reaction-diffusion library retrieves k^*_{on} and k_{off}. For very large dissociation rates, only a lower limit can be calculated, which is determined by the time resolution of 3PEA. In the current implementation, it is limited by the error of the bleach time assignment, which is roughly 50 μs. Thus, dissociation rates up to about 10,000 s^{-1} can be resolved.

1. Sprague BL, Pego RL, Stavreva DA, McNally JG (2004) Analysis of binding reactions by fluorescence recovery after photobleaching. *Biophys J* 86(6):3473–3495.
2. Michelman-Ribeiro A, et al. (2009) Direct measurement of association and dissociation rates of DNA binding in live cells by fluorescence correlation spectroscopy. *Biophys J* 97 (1):337–346.
3. Soumpasis DM (1983) Theoretical analysis of fluorescence photobleaching recovery experiments. *Biophys J* 41(1):95–97.
4. Ortega A, Amorós D, García de la Torre J (2011) Global fit and structure optimization of flexible and rigid macromolecules and nanoparticles from analytical ultracentrifugation and other dilute solution properties. *Methods* 54(1):115–123.
5. Görisch SM, Wachsmuth M, Tóth KF, Lichter P, Rippe K (2005) Histone acetylation increases chromatin accessibility. *J Cell Sci* 118(Pt 24):5825–5834.
6. Pack C, Saito K, Tamura M, Kinjo M (2006) Microenvironment and effect of energy depletion in the nucleus analyzed by mobility of multiple oligomeric EGFPs. *Biophys J* 91(10):3921–3936.
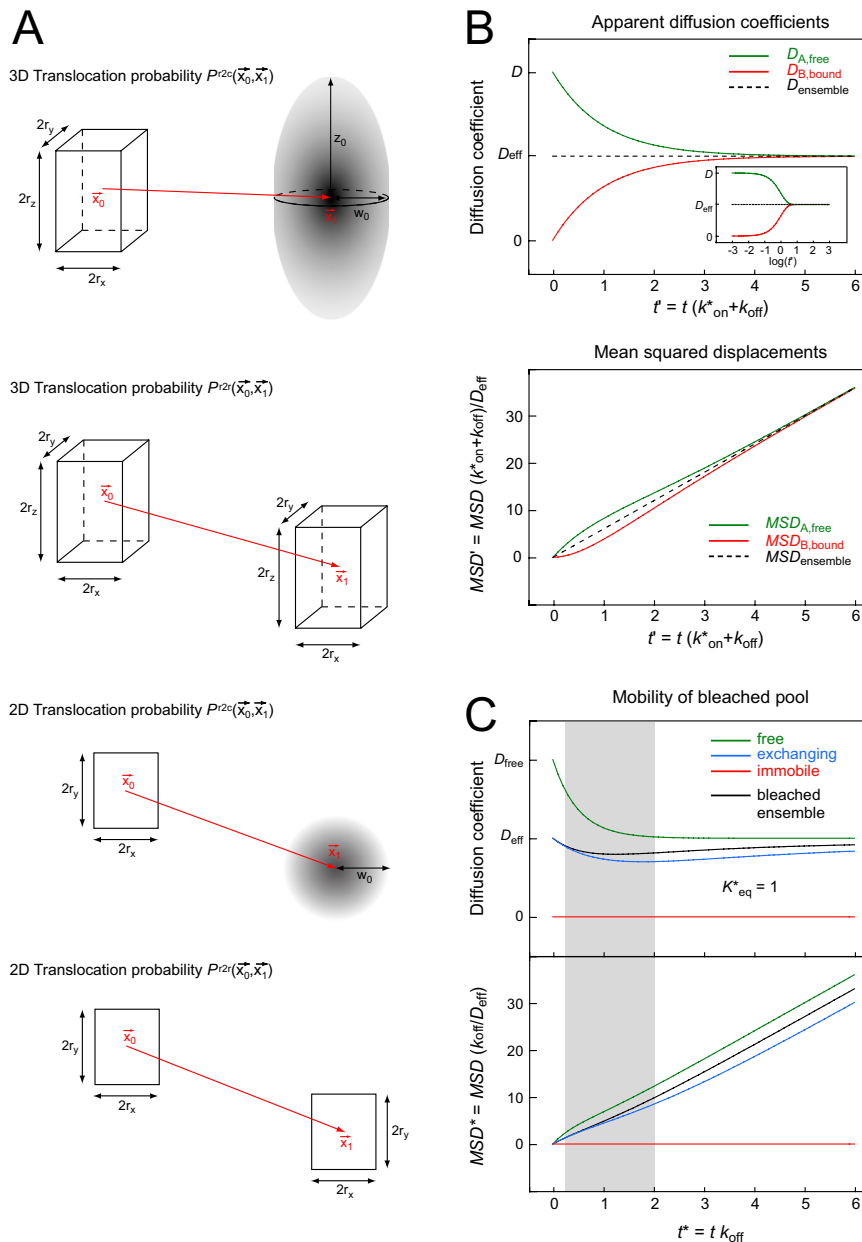
Fig. S1. Function definitions and behavior of reaction-diffusion processes. (*A*) Translocation probabilities used for the derivation of the theoretical 3PEA framework are visualized. P^{r2r} is the translocation probability between two cubes or rectangles, P^{r2c} is the translocation probability between a cube and a 3D-Gaussian distribution or a rectangle and a 2D-Gaussian distribution. (*B*) The scale-dependent behavior of reaction-diffusion processes is illustrated, and the time-dependent apparent diffusion coefficients for the particles that are initially free or bound are shown. (*C*) The bound pool can be further subdivided into an immobile pool (bound longer than t^*) and an exchanging pool (bound shorter than t^*) according to the propagator in Eq. **8**. On different scales, different pools are present, allowing for retrieval of distinct observables. For very short measurement scales, only an immobile fraction and a mobile fraction diffusing with D are present; for very large measurement scales, only one pool diffusing with D_{eff} is present. In both cases, the individual rate constants are not obtained. Rather, measurements on the intermediate time scale have to be conducted to characterize the process fully.
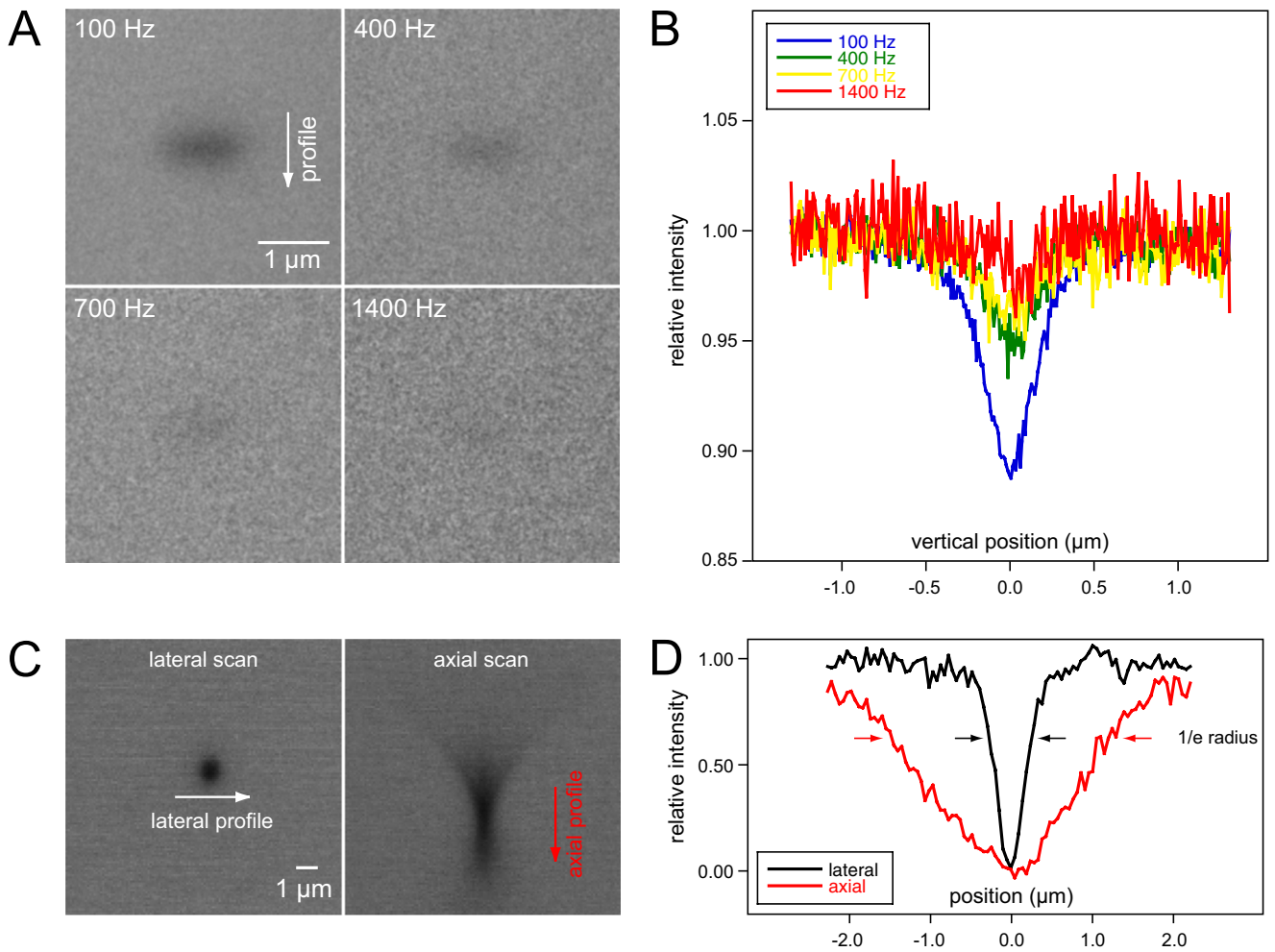
Fig. S2. Calibration of the bleach PSF. The bleach PSF in lateral and axial direction was determined with a GFP solution dried on a coverslip and a fluorescent plastic slide (Chroma Technology Corp.), respectively. (*A*) Line segments were bleached with different scan speeds to obtain the lateral geometry of the bleach PSF from the dried GFP sample. (*B*) Intensity perpendicular to the bleached line segments from *A* was plotted to determine the effective bleach depth. (*C*) A spot was bleached on the chroma slide to determine the axial geometry of the bleach PSF. (*D*) Intensity profiles from *C* were plotted to estimate the beam waist for the bleach PSF.
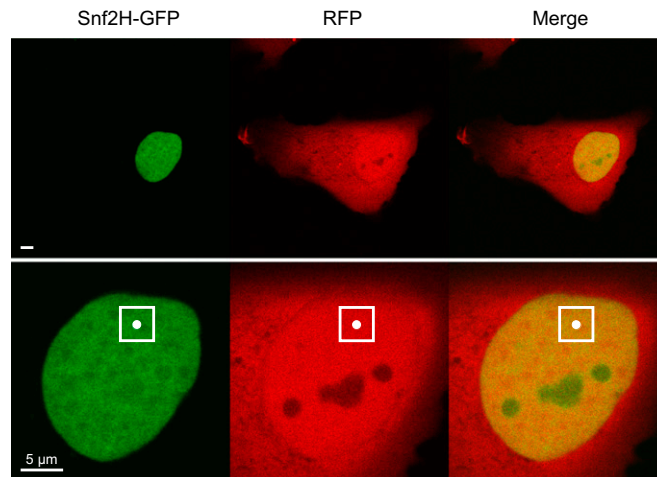
Fig. S3. Representative cell coexpressing Snf2H-GFP and red fluorescent protein (RFP). U2OS cells stably expressing Snf2H-GFP were transiently transfected with a plasmid coding for TagRFP. The bleach region was positioned in a region of the nucleoplasm where both proteins were mostly homogeneously distributed.
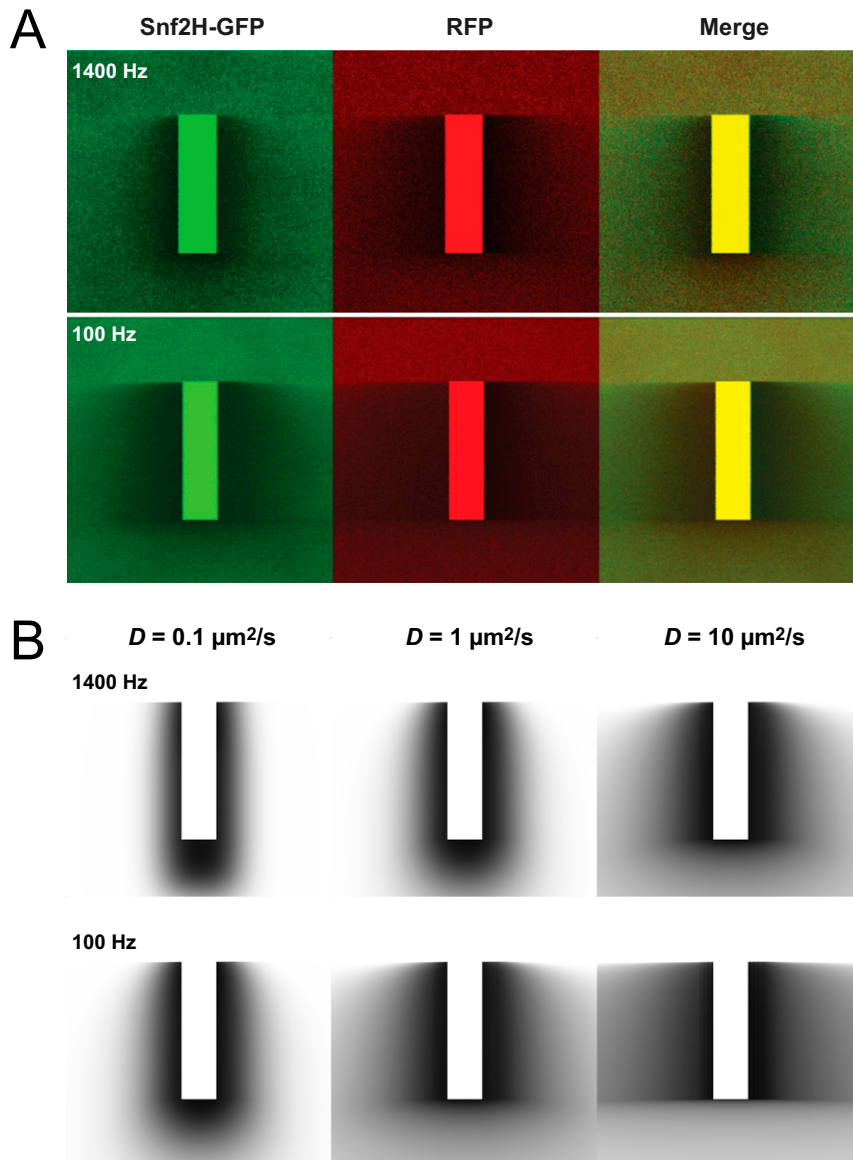
Fig. S4. Experimental implementation of 3PEA for a rectangular bleach region. (*A*) A stable Snf2H-GFP U2OS cell line was transfected with free red fluorescent protein (RFP) (Fig. S3), and the mobilities of both proteins were measured in a 3PEA experiment. Scan speeds of 100 Hz and 1,400 Hz were used for raster acquisition and bleaching. The rectangular bleach regions had dimensions of 2 μm × 0.5 μm (experiments with a circular bleach geometry are shown in Fig. 2). As expected, the bleach coronas became broader for increasing diffusion coefficients and decreasing scan speeds. In the merge images, the less mobile protein can be readily identified by visual inspection of the predominant color in the area adjacent to the bleach region (here, Snf2H-GFP in green). (*B*) Exemplary theoretical bleach profiles for different diffusion coefficients calculated for the parameters used in the experiments, with 512 × 512 pixels and 7.5-nm voxel size. The experimental Snf2H-GFP profile seems to be most similar to the $D = 1$ μm²·s⁻¹ case, whereas the RFP profile is better approximated with $D = 10$ μm²·s⁻¹.
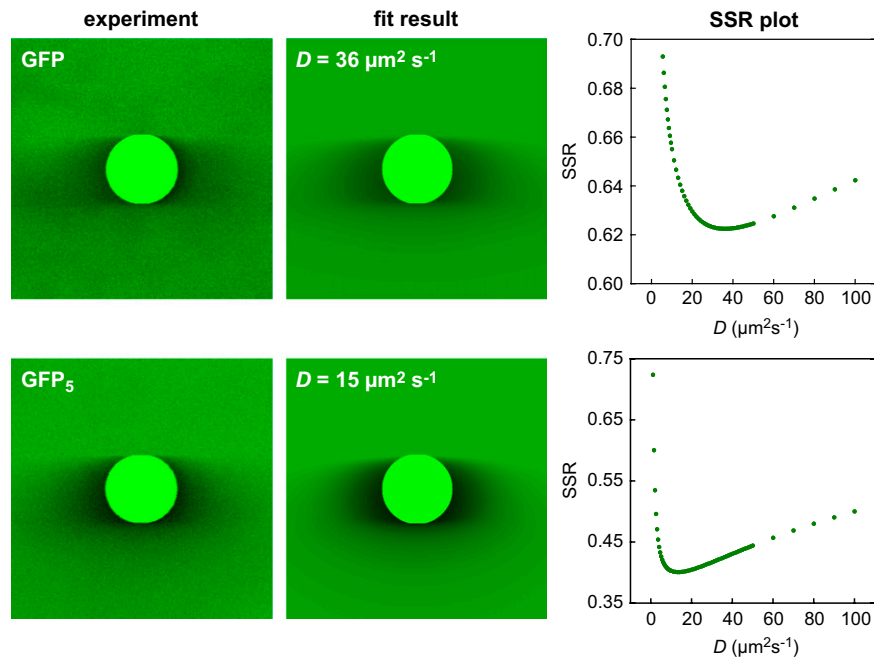
Fig. S5. Diffusion coefficient of free GFP and a GFP pentamer (GFP$_5$) measured by 3PEA in the nucleus. U2OS cells stably expressing free GFP or GFP$_5$ were subjected to 3PEA. Diffusion coefficients of $D = 36 \pm 5$ $\mu m^2 \cdot s^{-1}$ and $D = 15 \pm 2$ $\mu m^2 \cdot s^{-1}$ were determined for GFP and GFP$_5$, respectively. The experimental fluorescence intensity profile, the corresponding image for the best fit, and the sum of squared residuals (SSR) plot are shown.
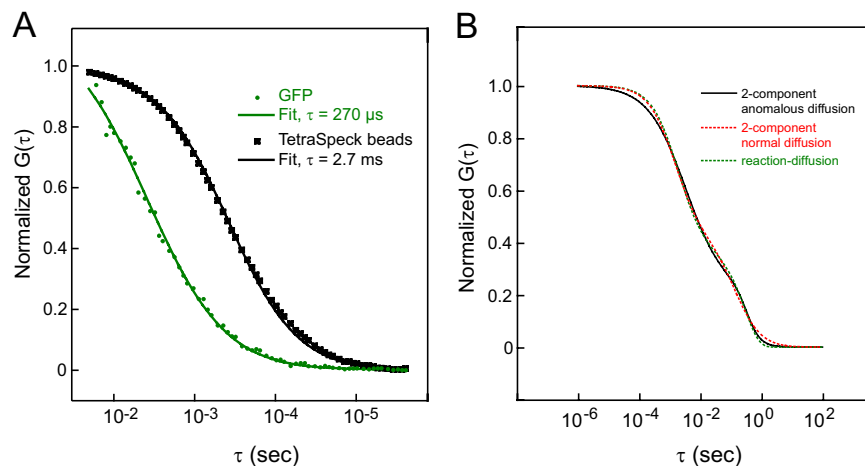
Fig. S6. Experimental calibration of fluorescence correlation spectroscopy (FCS) measurements and comparison of different FCS fit models. (*A*) Diffusion times of GFP and TetraSpeck 100 beads. The dwell time of free GFP expressed in U2OS cells was measured by FCS. As a reference, TetraSpeck beads with a diameter of 100 nm and a known diffusion coefficient of $D = 4.4$ $\mu m^2 \cdot s^{-1}$ were measured in aqueous solution. From the dwell time difference, an effective diffusion coefficient of $D = 44$ $\mu m^2 \cdot s^{-1}$ was determined for GFP. (*B*) FCS autocorrelation curves for reaction-diffusion processes (green) have a very similar shape as autocorrelation curves with two diffusive components (red). Thus, it is difficult to decide if the second component originates from jiggling of the chromatin fiber or from a reaction-diffusion process with an immobile substrate. For comparison, the best fit of a two-component anomalous diffusion model to an experimental curve for Snf2H-GFP is shown (black). Curves were plotted according to the equations in the studies by Michelman-Ribeiro et al. (1) and Erdel et al. (2) with the parameters for two-component anomalous diffusion ($D_{fast} = 6$ $\mu m^2 \cdot s^{-1}$, $D_{slow} = 0.06$ $\mu m^2 \cdot s^{-1}$, $\alpha_{fast} = 0.7$, $\alpha_{slow} = 2.0$, $f_{fast} = 0.78$), two-component normal diffusion ($D_{fast} = 15$ $\mu m^2 \cdot s^{-1}$, $D_{slow} = 0.16$ $\mu m^2 \cdot s^{-1}$, $f_{fast} = 0.57$), and reaction-diffusion ($K^*_{eq} = 0.59$, $k_{off} = 3.2$ s^{-1}, $D = 12$ $\mu m^2 \cdot s^{-1}$).

1. Michelman-Ribeiro A, et al. (2009) Direct measurement of association and dissociation rates of DNA binding in live cells by fluorescence correlation spectroscopy. *Biophys J* 97(1): 337–346.
2. Erdel F, Schubert T, Marth C, Längst G, Rippe K (2010) Human ISWI chromatin-remodeling complexes sample nucleosomes via transient binding reactions and become immobilized at active sites. *Proc Natl Acad Sci USA* 107(46):19873–19878.
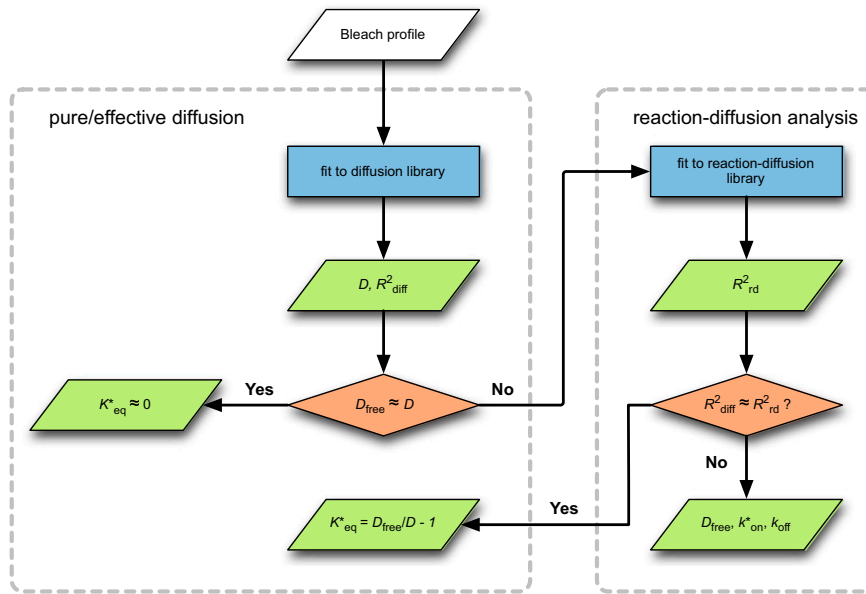
Fig. S7. Workflow for 3PEA. The general workflow for the mobility analysis of different proteins by 3PEA is shown. Based on this methodology, the effective diffusion coefficient for the proteins can be determined. Furthermore, the binding interactions between the protein and immobile obstacles can be characterized as described in the main text and *SI Text*.
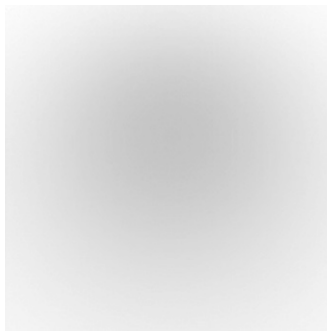

Movie S1. Simulated bleach experiment with $D = 1\ \mu m^2 \cdot s^{-1}$. Confocal light scanning microscopes acquire and bleach images via a raster scan process. Pixels are sequentially illuminated from the upper left pixel to the lower right pixel. In the standard unidirectional mode, all lines are scanned from left to right. Thus, after a line has been scanned, the microscope's illumination beam moves to the left pixel of the next line ("fly-back"). (*Left*) Current beam position is depicted. During fly-back, a gray strip appears in the lower left corner. The bleach region consists of one pixel located in the center of the image. When the illumination beam reaches this pixel, the intensity increases and a Gaussian-shaped profile is bleached into the pool of fluorescent particles. (*Center*) Current intensity distribution that could be observed by looking at all particles simultaneously is depicted (fluorescent particles are represented in white, bleached particles are represented in black). The intensity distribution does not correspond to the acquired image, because the microscope detects only one pixel at a time at the point where the illumination beam is located (*Left*), which leads to the CLSM image (*Right*). The bleach profile is asymmetrical, because the pixels above the bleach region are acquired before bleaching has occurred and because diffusion takes place during the acquisition process. For the simulation, a voxel size of 100 nm, a pixel dwell time of 5 μs, and a diffusion coefficient of $1\ \mu m^2 \cdot s^{-1}$ were used.

[Movie S1](#)
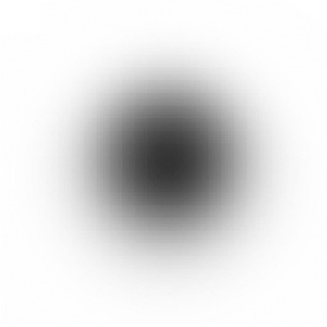
Movie S2. Simulated bleach experiment with D = 10 $\mu m^2 \cdot s^{-1}$. The bleach experiment is the same as in Movie S1 but with a diffusion coefficient of 10 $\mu m^2 \cdot s^{-1}$. Diffusion during the bleach process is evident, leading to a bleach profile that is broadened in its lower part.

Movie S2

Movie S3. Simulated bleach experiment with D = 100 $\mu m^2 \cdot s^{-1}$. The bleach experiment is the same as in Movie S1 but with a diffusion coefficient of 100 $\mu m^2 \cdot s^{-1}$. Here, diffusion occurring during the bleach process is significant. The bleach profile becomes very broad at its lower part, and the remaining bleach depth after completion of the image frame is very small. Thus, the signal would be insufficient for a conventional FRAP analysis.

Movie S3